

PAPER • OPEN ACCESS

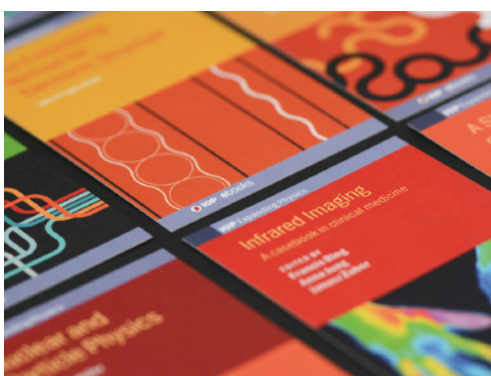
## Investigation of the effect of structural defects from hydride precipitation on superconducting properties of high purity SRF cavity Nb using magneto-optical and electron imaging methods

To cite this article: Mingmin Wang *et al* 2022 *Supercond. Sci. Technol.* **35** 045001

View the [article online](#) for updates and enhancements.

You may also like

- [First-principles calculations of niobium hydride formation in superconducting radio-frequency cavities](#)  
Denise C Ford, Lance D Cooley and David N Seidman
- [Theoretical estimates of maximum fields in superconducting resonant radio frequency cavities: stability theory, disorder, and laminates](#)  
Danilo B Liarte, Sam Posen, Mark K Transtrum *et al.*
- [Electron bunch train excited higher-order modes in a superconducting RF cavity](#)  
Yong-Feng Gao, , Sen-Lin Huang *et al.*



**IOP | ebooks™**

Bringing together innovative digital publishing with leading authors from the global scientific community.

Start exploring the collection—download the first chapter of every title for free.

# Investigation of the effect of structural defects from hydride precipitation on superconducting properties of high purity SRF cavity Nb using magneto-optical and electron imaging methods

Mingmin Wang<sup>1</sup> , Anatolii Polyanskii<sup>2</sup> , Shreyas Balachandran<sup>2</sup> , Santosh Chetri<sup>2</sup>, Martin A Crimp<sup>1</sup>, Peter J Lee<sup>2</sup>  and Thomas R Bieler<sup>1,\*</sup> 

<sup>1</sup> Michigan State University, Chemical Engineering and Materials Science, East Lansing, MI 48824, United States of America

<sup>2</sup> National High Magnetic Field Laboratory-Applied Superconductivity Center, Florida State University, Tallahassee, FL, 32310, United States of America

E-mail: [bieler@egr.msu.edu](mailto:bieler@egr.msu.edu)

Received 20 May 2021, revised 25 January 2022

Accepted for publication 27 January 2022

Published 14 February 2022



CrossMark

## Abstract

Nb is an elemental superconductor with a critical temperature of 9.3 K and is widely used to fabricate superconducting radiofrequency (SRF) cavities for particle accelerators. However, microstructural defects in Nb, such as grain boundaries (GBs) and dislocations, can act as pinning centers for magnetic flux that can degrade SRF cavity performance. Hydrogen contamination is also detrimental to SRF cavity performance due to the formation of normal conducting hydrides during cool down. In this study, disc shaped Nb bi-crystals extracted from high-purity large-grain Nb slices were investigated to study the effects of GBs, hydrogen, and dislocations on superconducting properties. Grain orientation and GB misorientation were measured using Laue x-ray diffraction and electron backscattered diffraction (EBSD) analyses. Cryogenic magneto-optical imaging was used to directly observe magnetic flux penetration below  $T_c = 9.3$  K. Damage caused by low temperature precipitation of hydrides and their dissolution upon reheating after cryogenic cycles was examined using electron channeling contrast imaging, and EBSD. The relationships between hydride formation, dislocation content, GBs, cryo-cooling, heat treatment (HT), and flux penetration indicate that both GB character and hydrogen content affect magnetic flux penetration. Such flux penetration could be facilitated by dislocation structures and low angle GBs resulting from hydride precipitation and HT.

\* Author to whom any correspondence should be addressed.



Original content from this work may be used under the terms of the [Creative Commons Attribution 4.0 licence](https://creativecommons.org/licenses/by/4.0/). Any further distribution of this work must maintain attribution to the author(s) and the title of the work, journal citation and DOI.

Keywords: pure niobium, grain boundaries, magnetic flux pinning, niobium hydrides, dislocation substructure, magneto-optical imaging, electron channeling contrast imaging

(Some figures may appear in colour only in the online journal)

## 1. Introduction

Superconducting radio-frequency (SRF) cavities used for charged particle accelerators are usually made from high purity Nb because of its highest critical temperature ( $T_c = 9.3$  K) among elemental superconductors, its high critical magnetic field, as well as its good formability, reliable chemical stability, and sufficient market availability [1, 2]. Pushing the limits of a high accelerating field and a high quality factor (Q) provides the motivation for continuing research and development of Nb cavities. Over the past decades, improvements in the fabrication process have enabled the theoretical accelerating field limit of about  $52 \text{ MV m}^{-1}$  to be achieved [3]. While quality factors have reached  $\sim 10^{11}$  [4], this cannot be consistently reproduced when using the same manufacturing processes, suggesting variability within the material. Dislocations and grain boundaries (GBs) introduced during fabrication paths are among the defects that limit SRF cavity performance. Chemical removal of the surface damage introduces hydrogen that can form normal conducting hydrides when cooled to cryogenic temperatures. Dislocations, GBs, and normal conducting hydrides can facilitate magnetic flux trapping and perturb the superconducting currents and increase residual resistance [5–21]. Defects can be flux traps in a superconductor as it cooled below  $T_c$ , where an ideal superconductor would be diamagnetic and flux free [14].

This study focuses on three kinds of defects: dislocations, GBs and hydrogen. Dislocations can facilitate flux entry and are capable of trapping magnetic flux, resulting in radio frequency (RF) losses due to oscillatory motion of trapped flux under RF fields [6, 7, 15, 21]. Previous work shows that GBs are weak links and show lower critical current density than bulk material [22]. GBs oriented parallel to external magnetic fields can cause preferential flux penetration [23–25]. More recently, flux penetration along low angle grain boundaries (LAGBs) was also observed in single-crystal Nb samples [19, 26, 27]. In a sample deformed and heat treated to yield regions of small and large grain size, poor flux expulsion and trapped flux occurred in small-grain regions [27]. Hydrogen can easily enter Nb during electro-polishing or buffered chemical polishing (BCP) when the original oxide layer is removed [28], causing normal-conducting Nb hydride precipitation during cooling. Precipitation causes a 12% volume increase, which is accommodated by elastic strain and formation of dislocation loops that transport material away from the hydrides [29–36]. Although hydrides dissolve during heating, the plastic deformation caused by them is not reversible, leaving scars with locally high dislocation densities in regions where hydrides were

present [29, 30, 34]. Magnetic flux trapping by hydrides has been observed using magneto-optical (MO) imaging [37].

The issue of Q-drop in SRF cavities, a sharp decrease in quality factor Q at high surface magnetic fields of 900–1000 Oe, is well-known [15, 21]. Low temperature baking has been shown to reduce high field Q-drop, possibly due to dislocation annihilation during baking [21]. Suppression of hydride formation [35] by nitrogen doping/infusion has been used to engineer the surface layer of Nb to reduce Q-drop and significantly boost the quality factor [38–40]. Recent research [4, 41, 42] on magnetic flux expulsion shows that nearly full flux expulsion and ultra-high quality factors ( $\sim 10^{11}$ ) can be achieved by high temperature heat treatments (HTs) combined with intentionally imposed thermal gradients during cooling. However, a systematic study on the flux trapping mechanisms responsible for these observations at the microscopic level is still lacking.

In the present work, flux penetration and trapping are investigated in bi-crystal samples using cryogenic MO imaging, and the microstructure evolution due to hydride precipitation and subsequent HT is characterized using electron channeling contrast imaging (ECCI) and electron backscattered diffraction (EBSD). This work builds on preliminary observations from these samples in [26]. The goal is to identify relationships between hydride formation, dislocation content, GBs, cryo-cooling, HT, and flux penetration and trapping. These questions motivate the experimental design and research goals:

- (a) GBs, hydrogen, and flux penetration: Do hydrides facilitate GB flux penetration? If so, do the GBs favor hydride formation?
- (b) Dislocations, hydride formation, and flux penetration: Does hydride formation cause multiplication of dislocations, which in turn provides sites for flux trapping?

Three bi-crystal samples (Samples I, II, and III) were investigated, but the majority of insights come from Sample II, which is the focus of this paper. Samples I and III provide important details supporting the interpretation, and are described in the appendix.

The paper is organized as follows: section 2 describes the experimental procedures and techniques used in this study; section 3 presents the results of cryo-cycles and HTs on MO imaging of the magnetic flux behavior in chronological order, as well as microstructure analysis of both the surface and sub-surface of Sample II; section 4 discusses the findings and assesses the questions raised above, leading to further motivating hypotheses and opportunities for future work, and section 5 summarizes the findings.

## 2. Experimental methods

### 2.1. Orientation measurement and bi-crystal sample extraction

Samples for this study were taken from two SRF grade large grain 270 mm cylindrical Nb ingot slices 3 mm thick from two vendors (Ningxia Orient Tantalum Industry Co. Ltd and Tokyo Denkai Co. Ltd). Laue x-ray diffraction was used to measure orientations of the grains, allowing determination of the misorientation across the visible GBs as described in [26]. Three bi-crystal cylindrical samples were extracted using electrical discharge machining (samples I and II from the Ningxia Nb slice and Sample III from the Tokyo Denkai Nb slice) such that the GB bisected the sample with the sample axis parallel to the original Nb ingot axis. Each sample was sliced into two discs about 1.3 mm thick, which were subsequently processed by both vibratory polishing and light BCP to obtain a smooth surface for electron microscopy and MO analysis, leading to a diameter of 2.84 mm, and a thickness of 0.79 mm in sample II, and the boundary misorientation is 24° (details about samples I and III are in table A1 in the appendix). The optical image in figure 1(a) shows the visible GB trace on the top surface, while the GB trace on the bottom surface is indicated by a dashed line. The inclination between the GB and surface varied from 90° (in the right 2/3 of the boundary) to about 82° (in the left 1/3 of the boundary, figure 1(a)).

### 2.2. Cryogenic MO imaging and critical current density estimation

The MO technique enables both local and global magnetic flux behavior to be visualized using the double Faraday effect in a garnet indicator film sitting directly on the sample surface. In these experiments, the samples are situated at the center of a solenoid which can generate magnetic fields up to 1200 Oe; reported fields generated by the coil at the sample are calibrated values based upon the current in the solenoid [24]. In the reflective mode with in-plane magnetization, the relationship between microstructural defects and magnetic flux penetration and trapping below the 9.3 K critical temperature ( $T_c$ ) is directly visualized with an optical microscope [23, 43–47]. While this method was developed for thin films, it has been adapted for thicker samples with an iterative procedure such that aspect ratios of diameter to thickness as low as 3 can provide a resolution of about 30  $\mu\text{m}$  [46]. There are three imaging modes: zero-field-cooling (ZFC) mode, remnant field (RF) mode, and field-cooling (FC) mode [19, 24, 45]. For the ZFC mode, the sample was cooled in a zero magnetic field below  $T_c$ , and then the external magnetic field was increasingly applied perpendicular to the sample surface. In MO images, flux penetration from the perimeter into the sample is revealed as bright contrast (dark regions are in the Meissner state and flux-free). For the RF mode, the external field was removed to show the remnant (trapped) field within the sample. In the FC mode, the sample was cooled in an external field above  $T_c$ , and then the external field is removed after reaching a temperature below  $T_c$  to form the FC MO image. In comparison to the ZFC mode,

which is sensitive to surface superconducting properties, the FC MO images show mostly bulk flux trapping properties. A disc-shaped MO sample was used to avoid the influence of corners on the flux distribution [24].

The critical current density ( $J_c$ ) of a superconductor is the maximum current density a superconductor can carry before transitioning to the normal conducting state, and it is proportional to the flux pinning force density described in equation (1) [14]:

$$J_c = \frac{F_p}{B} \quad (1)$$

where  $F_p$  is the pinning force density, and  $B$  is the magnetic flux density. Critical current density can be estimated from MO images by measuring the width of the flux-free Meissner regions [45]. GB transparency ( $r$ ) is defined as the ratio of the critical current density across the GB  $J_c^{GB}$  to that within the grain (bulk)  $J_c^{grain}$  [43, 47]:

$$r = \frac{J_c^{GB}}{J_c^{grain}}. \quad (2)$$

This GB transparency can be calculated from the MO images, as discussed in [43]. A GB transparency less than 1 indicates weaker flux pinning at the GB in comparison to the adjacent grains. In other words, the GB becomes less resistant to flux penetration compared to the grain.

### 2.3. EBSD orientation mapping

EBSD scans of etched sample surfaces were performed on a Tescan Mira field emission gun-SEM equipped with an EDAX Hikari EBSD camera (480 × 480 pixel resolution) and an orientation imaging microscopy (OIM) software, using step sizes less than 1  $\mu\text{m}$ . A voltage of 25 kV, working distances of 20–25 mm, and an exposure time of 0.1 s were used. Inverse pole figure (IPF), image quality (IQ), Kernel average misorientation (KAM), and grain reference orientation deviation-angle (GROD-angle) and -axis (GROD-axis) maps were generated using OIM analysis software v. 7.3.1 after one round of neighbor confidence index cleanup.

### 2.4. Dislocation density mapping using HR-EBSD analysis

High-resolution (HR) EBSD cross-correlation analysis was performed using the MATLAB-based OpenXY software [48] to measure and map the geometrically necessary dislocation (GND) density. A spot size of 20 nm and a specimen current of 1.9 A were used for collection of high quality EBSD patterns necessary for cross-correlation analysis, using the same SEM and parameters described above.

### 2.5. Heat Treatment (HT) and nitrogen infusion

HTs were done in a vacuum furnace at the Jefferson National Accelerator Facility, where samples were included with cavity HTs. The samples were heated at a rate of 5 °C min<sup>-1</sup>–800 °C under an ultra-high vacuum condition, which was maintained for 3 h, followed by furnace cooling to 175 °C. Sample II went

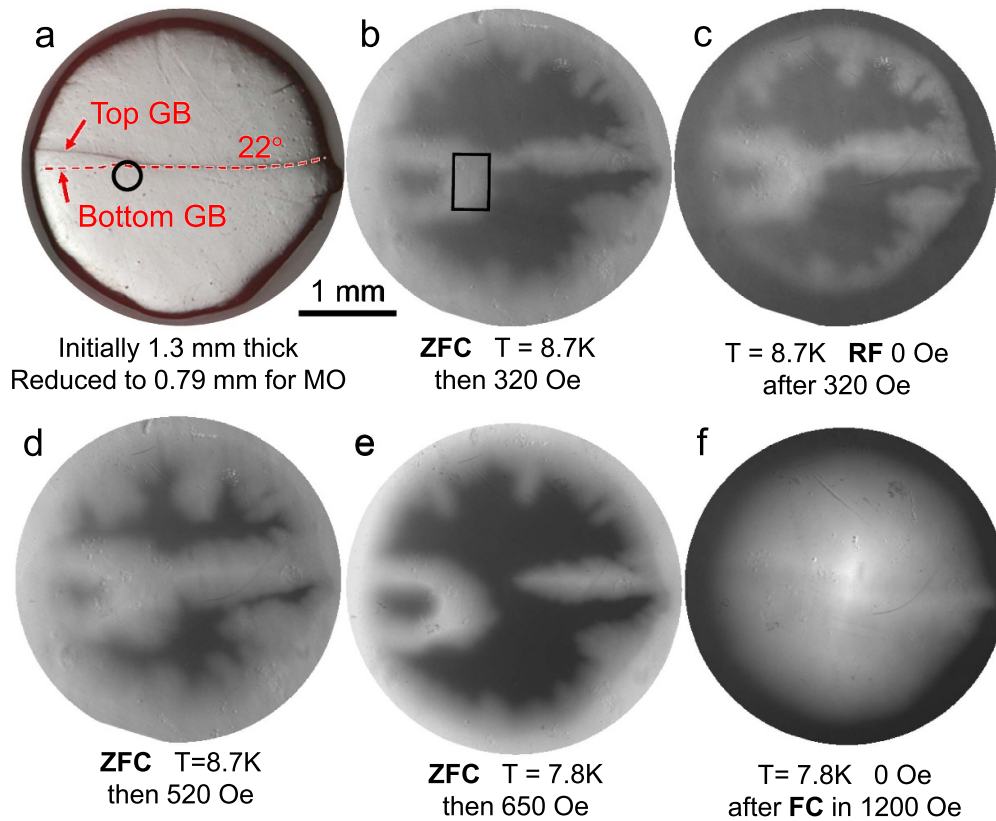


**Figure 1.** (a) Optical image showing locations of GBs on the top and the bottom surface (dashed line) and sequential MO images taken at 8.7 K (b)–(d) and 7.8 K (e) and (f). The black circle in (a) indicates the location where ECCI imaging was performed. The black rectangular outline in (b) indicates the area examined using EBSD in figure 2.

through a nitrogen infusion cycle at 175 °C in 25 mTorr nitrogen gas for 48 h after the prior 800 °C HT [49].

### 2.6. Electron channeling contrast imaging (ECCI)

Samples were prepared for ECCI [50, 51] by chemically removing material from the surface using BCP (25% nitric acid, 25% hydrofluoric acid, and 50% phosphoric acid). ECCI was conducted in the Tescan MIRA, which is equipped with beam rocking capability that allows selected area channeling patterns to be collected from areas of  $\sim 20 \mu\text{m}$  diameter. Specific (2-beam like) channeling conditions were obtained based upon known EBSD orientations in conjunction with the TOCA software (Tools for Orientation determination and Crystallographic Analysis) [52, 53].

## 3. Results

Results of Sample II are presented in the main text of the paper, while those of Samples I and III are described in the appendix.

### 3.1. Initial MO imaging observations

The MO results of sample II are shown in figure 1. MO observations were performed at 8.7 K and then repeated at 7.8 K after reheating above  $T_c$  to about 15 K. The sample was first ZFC to 8.7 K, and then the external field was incrementally

increased, and ZFC MO images were taken. In an ideal defect-free disc shaped sample, flux should penetrate from the perimeter inward as a bright ring squeezing a flux-free dark Meissner zone [24]. However, in real superconductors, defects such as precipitates and GBs distort the ideal flux penetration pattern by providing additional channels such as the features shown in figure 1. A ‘fork’ shaped flux penetration along the 22° high angle grain boundary (HAGB) and along a  $\sim 2^\circ$ – $3^\circ$  LAGB commenced at a field just below 300 Oe, and is shown in the first ZFC image in figure 1(b) at 320 Oe (at 300 Oe, the flux had not penetrated to the center). After removing the 320 Oe external field, the resulting RF image in figure 1(c) shows that the magnetic flux was trapped and did not exit the superconductor. The field was then increased again to examine the evolution of the flux penetration, which occupied more of the sample volume after increasing the field to 520 Oe, as flux penetrated inward from the perimeter and the GBs, illuminating about  $\frac{3}{4}$  of the area (figure 1(d)). The field was removed and the sample was then reheated to 15 K and again ZFC to a lower temperature of 7.8 K. The first flux penetration occurred from the edges along the same three boundary locations just below 540 Oe (the critical field of the superconductor increases parabolically with  $T/T_c$ , for  $T < T_c$ ). A field of 650 Oe (figure 1(e)) was required to cause flux penetration to a similar extent as figure 1(b). The sample was then reheated again to 15 K and subsequently FC to 7.8 K in an external field of 1200 Oe, where the field fully penetrated the whole sample. When the

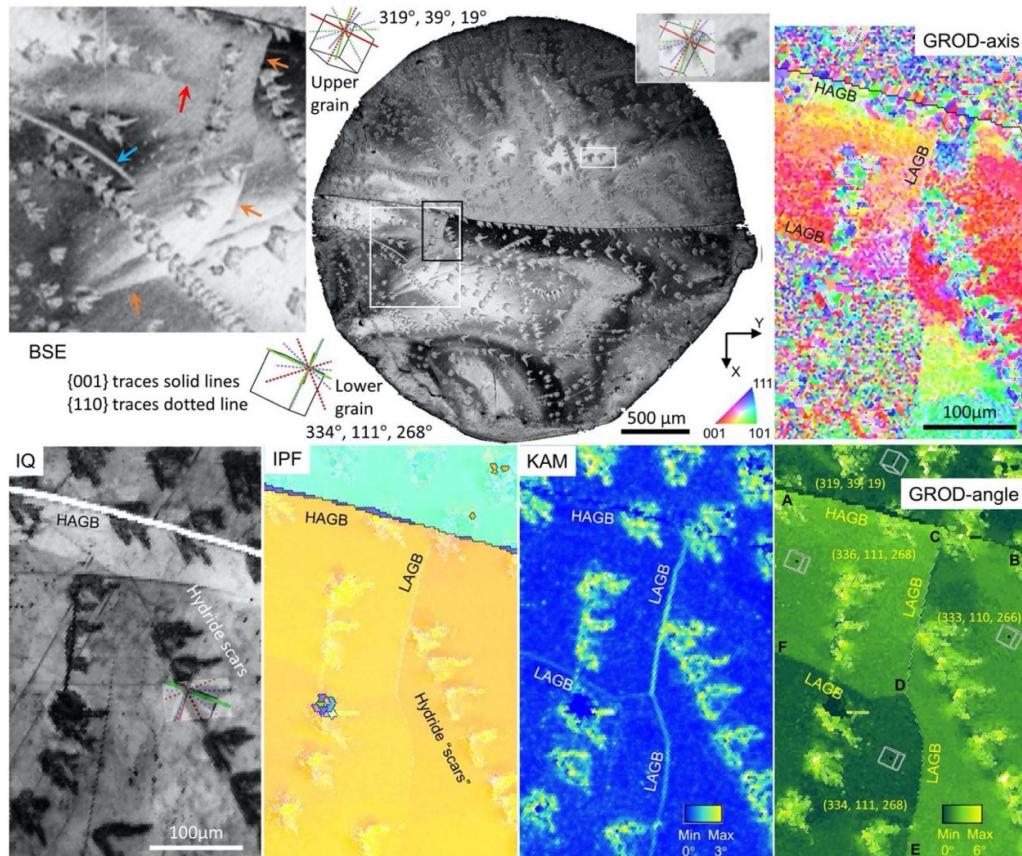


**Figure 2.** Backscattered electron (BSE) image (top left and top center) of the Sample II surface after the first MO cryogenic cycle shows a large number of  $\sim 50 \mu\text{m}$  hydride scars matching  $\{110\}$  plane traces (plotted as colored dotted lines on unit cells of both grains), arranged along some scratches and the HAGB. In the enlarged area outlined by the white box, orange arrows identify the curved LAGB observed in MO experiments (note abrupt contrast change across the LAGBs and no contrast change across scratches such as the one by the blue arrow). Additional details of the area in the black outline are shown in the EBSD maps; the IQ map indicates defects (dark features); the IPF map shows the HAGB (black line) and LAGBs ( $2^\circ$ – $15^\circ$ , white lines); the KAM map highlights LAGBs and hydride scars that caused local  $2^\circ$ – $3^\circ$  misorientations; the GROD-angle map is with respect to the average grain orientation indicated by Bunge Euler angles noted next to the prisms (based upon the identified X-Y coordinate system); the GROD-axis rotation axis map reveals different rotation axes in different subgrains. The IQ and the IPF maps from figure 4 in [26] are provided here to facilitate comparison.

external field of 1200 Oe was removed at 7.8 K, the trapped magnetic flux in the whole volume of the sample is visible as bright contrast in figure 2(f).

### 3.2. Microstructure analysis

After the 1st MO imaging sequence above, the microstructure of sample II was characterized using SEM imaging and EBSD mapping as shown in figure 2. Abrupt discontinuities in BSE contrast (orange arrows in enlarged BSE image) arising from abrupt changes in crystal orientation indicate a LAGB (note that the scratches (blue arrow) do not cause such abrupt changes in contrast) [50, 51]. This LAGB is perpendicular to the HAGB, but then curves to the lower left. The position of this LAGB is consistent with the location of the flux branch in the ZFC MO images in figure 1.

The GB characteristics are summarized in table 1. In the EBSD IPF map, LAGBs are identified with white lines for misorientations greater than  $2^\circ$ . In the KAM map, the LAGB is thicker close to the HAGB where it has a higher  $3^\circ$

**Table 1.** Misorientations and rotation axes of boundaries in the GROD-angle map in figure 2.

GB ID	GB type	Misorientation angle	Rotation axis
AB	HAGB	$21.9^\circ$	$[-21, 17, -9]$
CD	LAGB	$3.1^\circ$	$[27, -8, -9]$
DE	LAGB	$2.1^\circ$	$[14, -13, -23]$
FD	LAGB	$2^\circ$	$[26, 1, 10]$

misorientation and is thinner farther below the HAGB where the misorientation is about  $2^\circ$ . There is an additional LAGB approximately parallel to the main GB (red arrow on the enlarged BSE image, but it is most evident on the GROD-angle map between letters F-D). There is no evidence of LAGBs in other regions. The GROD-axis map is color coded according to the rotation axis between each pixel and the average grain orientation. In regions with a speckled pattern, the local grain orientation is close to the average grain orientation, but there are distinct subgrains with a uniform color that are misoriented

by a rotation axis indicated by its color. The different colors imply that different LAGBs consist of different combinations of dislocations operating on different slip systems.

### 3.3. Nb hydride surface scars

Hydride scars are evident from the BSE image and EBSD maps in figure 2. These scars result from accommodation of deformation caused by hydride precipitation during cooling. A cross section of a different sample following a cryogenic cycle reveals that scars can extend  $\sim 30 \mu\text{m}$  from the surface into the bulk material (figure A2 in the appendix). The near-surface hydride scars apparently grew along  $\{110\}$  planes, as they are aligned with multiple  $\{110\}$  plane traces (dotted lines) overlaid on the IQ map and on the enlarged BSE image of two scars of the upper grain. Though the detailed shapes of each scar differ, the scars in each of the two grains grew on the same set of  $\{110\}$  planes. These scar morphologies are consistent with Schober's observation of dendritic hydride formation on low-index  $\{110\}$  and  $\{100\}$  planes in Nb after rapid cooling [35]. The hydride scars have lower (darker) values in the IQ map, suggesting that plastic deformation associated with hydride precipitation distorts the crystal lattice and EBSD patterns. These nominally  $50 \mu\text{m}$  scars cause local misorientations as large as  $3^\circ$ , as shown in the KAM map. The scars are frequently lined up along features that appear to be scratches (most evident in the IQ map) and along the HAGB, but in contrast to the MO images in figure 1, they are not present along the LAGBs in the KAM and the GROD maps. Some of the hydride scars do not appear to be correlated with either a scratch or the HAGB (such as the hydride scar at the bottom of the IQ map).

### 3.4. Effect of HT and re-polishing on flux penetration behavior

To examine how HT and polishing affect the flux penetration behavior, four MO imaging assessments were made after the four different steps listed below:

- after mechanical polishing (MP) and BCP (figures 1 and 3 column (i)),
- after  $800^\circ\text{C}$  HT +  $175^\circ\text{C}$   $\text{N}_2$  infusion (figure 3 column (ii)),
- after MP to re-introduce hydrogen (figure 3 column (iii)),
- after a second  $800^\circ\text{C}$  HT (figure 3 column (iv)).

The  $800^\circ\text{C}$  3-hour HT at step ii was similar to that currently used for cavity processing [27]. Two MO images are shown for each of the four MO cycles in order to illustrate how the trapped flux increased with applied field; the contours of current streamlines were calculated from the second row of MO images. The in-grain ( $J_c^{\text{grain}}$ ) and the cross-grain-boundary ( $J_c^{\text{GB}}$ ) critical current densities and the ratio of the two (called GB transparency) were calculated from the MO images and listed at the bottom of figure 3. The critical current density can be used as an indicator of the strength of flux pinning for the GB or the grain.

Figure 3(i) shows the initial flux penetration at 7.8 K at 54 and 560 Oe (the same MO cycle as in figure 1(e)). The current streamline contours are bent inward at the LAGB and at both ends of the HAGB, indicating current distortion caused by GBs that show flux penetration. Flux penetration into both LAGB and HAGBs are easier and deeper than into the bulk, indicating that  $J_c^{\text{GB}}$  is lower than  $J_c^{\text{grain}}$ . This is consistent with a low GB transparency ( $r = J_c^{\text{GB}}/J_c^{\text{grain}}$ ) of about 0.16–0.23.

However, after subsequent HT and  $\text{N}_2$  infusion (figure 3(ii)) that resulted in less hydride formation and less perimeter surface pinning,  $J_c^{\text{grain}}$  dropped to a low value that is comparable to  $J_c^{\text{GB}}$ , leading to a GB transparency of 0.88, close to 1. This resulted in the disappearance of MO contrast at GBs. The flux penetration started at the center, at a lower field than when GB flux penetration was observed, and gradually expanded to most of the sample with no current distortion by GBs in the streamline map. The removal of hydrogen significantly decreased surface pinning in the two grains.

To determine if perimeter surface pinning could be restored by the reintroduction of hydrogen, the sample was mechanically polished in a colloidal silica solution to reintroduce hydrogen (step iii). The ZFC image in figure 3(iii) revealed a partly restored flux penetration on the right end of the HAGB, where the GB is perpendicular to the sample surface. However, penetration along the left end of the HAGB was not observed. As the position of the lower GB is unchanged with removal of material, and the displacement of the HAGB boundary from top to bottom is about the same after the sample was thinned (right side of figure 3), the inclination of the left side of the HAGB is about  $68^\circ$  from the surface. This implies that in the material removed, the left side of the HAGB was inclined close to  $90^\circ$  from the surface, consistent with flux penetration in figures 1 and 3(i), and the lack of flux penetration along the left side of the HAGB after material was removed (figure 3(iii)), and also appendix figure A1 Sample I). In contrast, the LAGB showed restored flux penetration. After MP,  $J_c^{\text{grain}}$  was partly restored from 30 to  $20 \text{ kA cm}^{-2}$ , and the GB transparency was reduced to 0.4, which is higher than the 0.2 value observed in step i. The flux penetration along the GB started at a field of 400 Oe, which is lower than the 540 Oe field in step I, which reflects changes in the sample due to HT, MP and reintroduction of hydrogen. This reduced magnetic field and higher GB transparency suggests that damage accumulated after multiple processing steps.

After a subsequent  $800^\circ\text{C}$  3-hour HT, a 4th cryo-cycle resulted in an MO image (figure 3(iv)) showing a similar pattern to figure 3(ii), with very low surface pinning, so flux was spread out and no GB flux penetration was visible, but at a similar field as after annealing in step ii. Calculations of critical current density shown in figure 3 suggests that HT and reintroduction of hydrogen in Nb affects  $J_c^{\text{grain}}$  more significantly than  $J_c^{\text{GB}}$ . In the presence of hydride pinning centers,  $J_c^{\text{grain}}$  is almost an order of magnitude higher than  $J_c^{\text{GB}}$ . The near constant  $J_c^{\text{GB}}$  leads to disruption of the critical current in the Nb bi-crystal.

The repeated cryogenic cycles and HTs with MO imaging shows that the flux penetration along the HAGB and LAGB can be turned on and off by introducing hydrogen via MP and

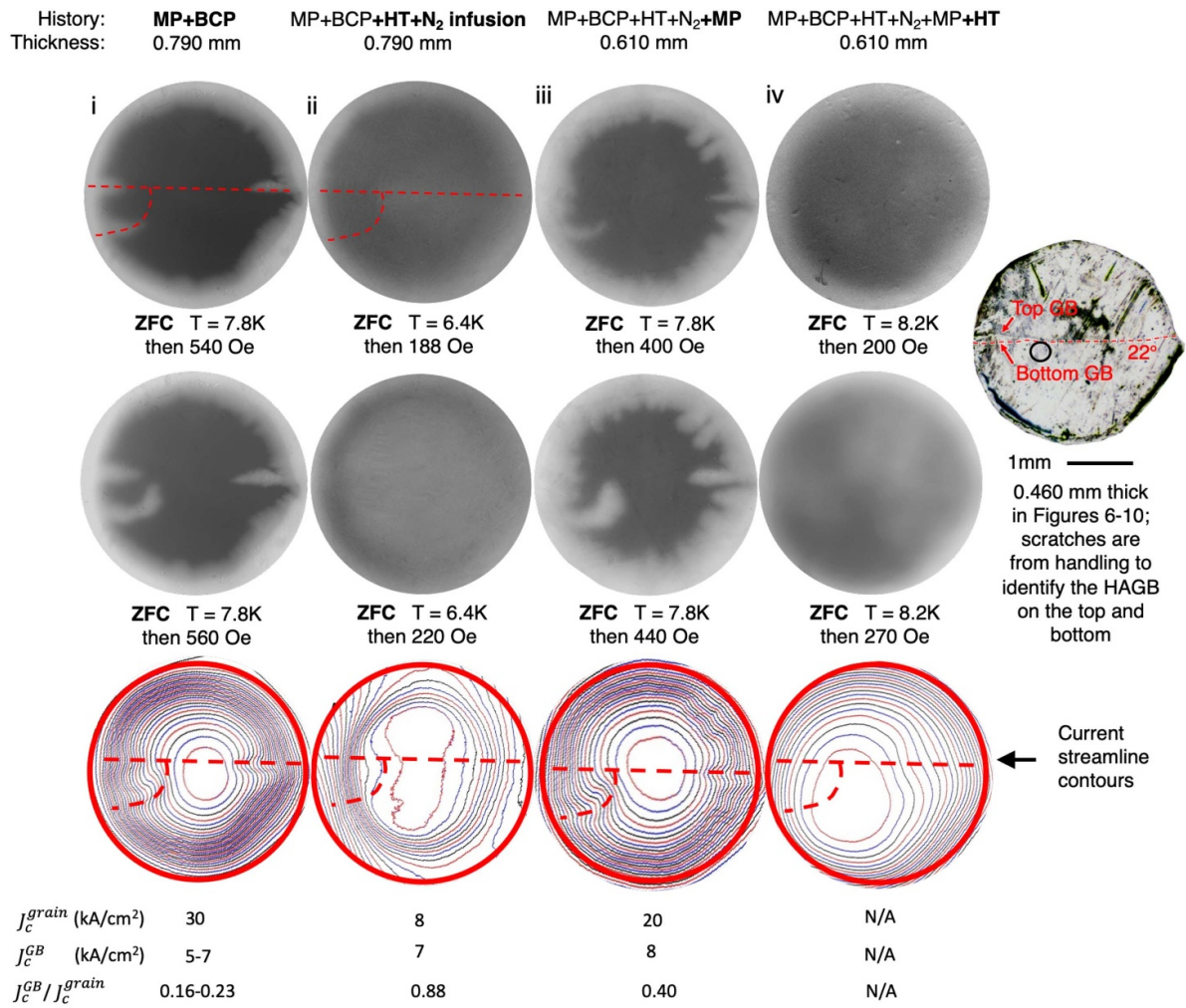


**Figure 3.** ZFC MO images from four MO cryo-cycles in columns: (i) first MO, (ii) after 800 °C 3-hour HT and nitrogen infusion, (iii) after subsequent MP to reintroduce hydrogen, and (iv) after a final 800 °C 3-hour HT. The location of the prior fork shape flux penetration is marked using red dashed lines. The contours of the calculated current streamline and critical current densities for each MO image are shown below the MO image. The current density is the highest at the circumference edge and decreases to zero in the flux free zone in the center. The colors of the streamlines are only for easy visualization. The MO image in column ii middle row is from figure 3(e) of [26], and has the correct 7.8 K temperature. Calculation of critical current density from column iv was not sufficiently reliable to report.

by removing hydrogen via HTs. Comparing MO images in figures 1 and 3, the field at which flux penetrates is very sensitive to temperature, so using the same temperature in all measurements would have been tidier, but this does not affect the interpretation of the observations. These observations show that damage caused by multiple processing steps cannot be fully restored even after HTs and that this flux penetration is directly correlated with the formation of hydrides.

### 3.5. Electron microscopy observations of hydride scars in the subsurface volume

Because the MO measurement in figure 1 reflects both a bulk and a surface effect, the subsurface region was examined after removing an additional 0.15 mm from the scar-covered surface after the four steps in figure 3, and shown in figure 4. In contrast to the surface observations in figure 2, the LAGB split into two boundaries as it approached the HAGB, indicating

that the LAGB is not perpendicular to the surface near the HAGB at this location. The BSE image shows three ~20 μm hydride scars (white arrows) along the nearly vertical LAGB, which are smaller than the ~50 μm hydride scars on the original surface in figure 2. Several hydride scars close to the HAGB are evident as ~3° local average misorientation regions on the KAM map. This is consistent with an observation of a large hydride that nucleated on a LAGB in prior work [30]. The KAM map also shows numerous ~1–5 μm regions with 2°–3° misorientations along the HAGB that may be small hydride scars. The GROD-angle map shows multiple subgrains near the LAGB-HAGB junction, which have different rotation axes represented by different colors in the GROD-axis map. The GROD-axis is more speckled with greater distance from the HAGB on both sides, but shows more uniform colors closer to the HAGB, indicating distinct rotation axes (with respect to the average orientation) in different subgrains near the HAGB.

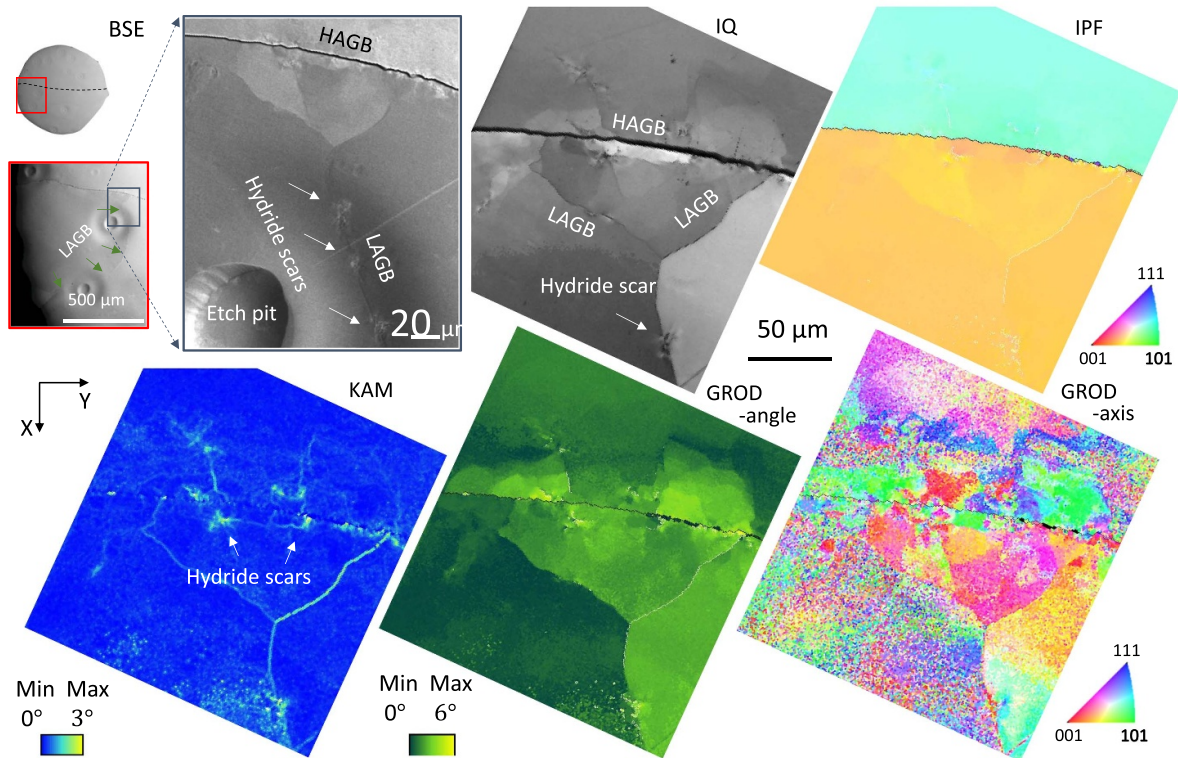


**Figure 4.** Subsurface in the fork flux penetration area (black outline in figures 1 and 2) after the four steps in section 3.4, and removal of about  $150\ \mu\text{m}$  shows hydride scars along both HAGB and LAGBs in the BSE image and EBSD maps. Multiple subgrains can be observed near the HAGB-LAGB junction in the GROD-angle and GROD-axis maps.

MO observations in figure 3 suggests that flux penetration along GBs is correlated with normal conducting hydride formation. This correlation could be due to either the property of the hydride itself or damage done by the formation of the hydrides. Consequently, the effect of internal strain resulting from hydride formation on defect formation was investigated using ECCI and EBSD.

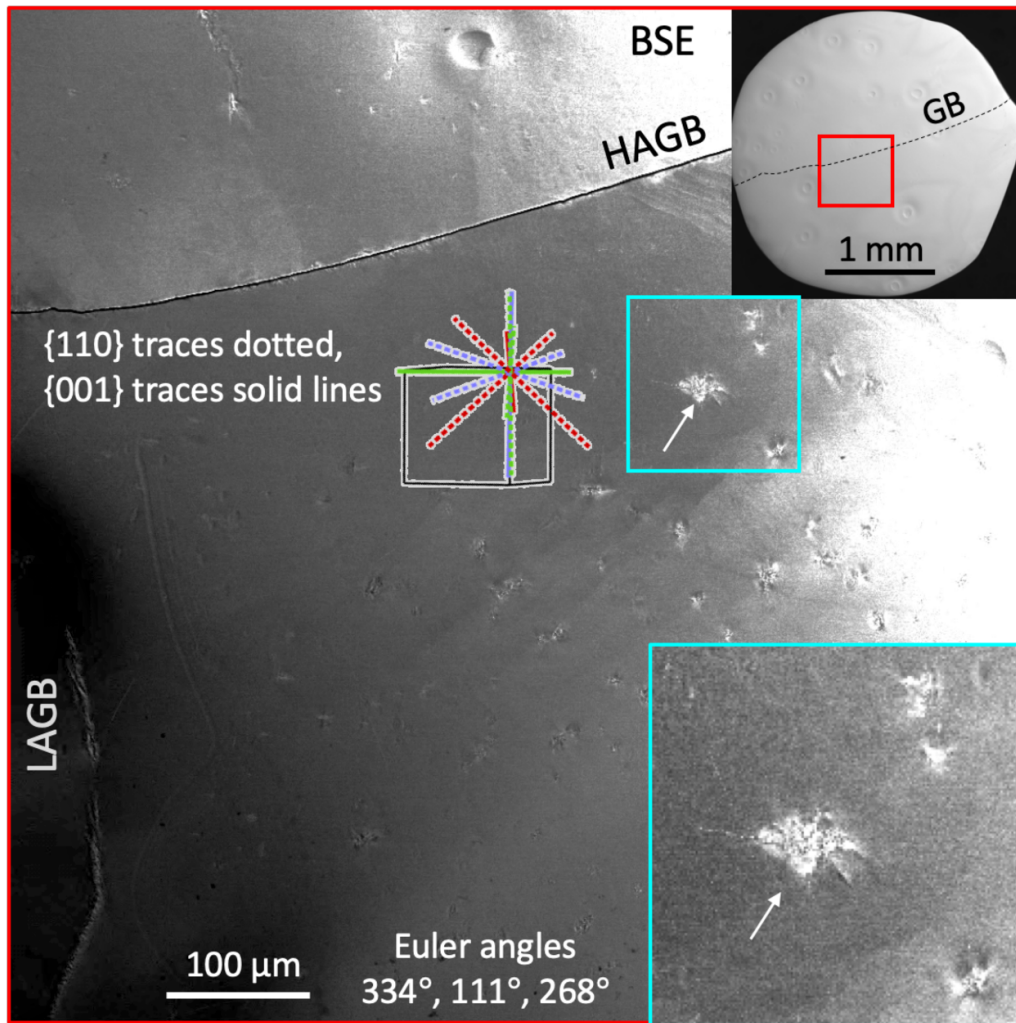
Figure 5 shows the BSE image of subsurface hydride scars and a specific scar (white arrow) was chosen for ECCI analysis in figure 6. Unlike the scars on the initial surface near the LAGB, which were aligned with  $\{011\}$  plane traces associated with scratches in figure 2, the major axes of the scar identified by the white arrow is aligned with  $\{001\}$  plane traces, as shown in the enlarged BSE inset image and the overlaid unit cell with colored plane traces (note the colors represent different planes in a crystal plane family).

Figure 6 (top left) shows an electron channeling contrast image of the scar identified by the white arrow in figure 5, under the channeling condition of  $\mathbf{g} = (\underline{2}00)$ . It shows the tips of the scar aligned with the  $\{100\}$  plane traces, but there are scar features between these axes that are also aligned with  $\{110\}$  traces. Enlarged images from three dashed box regions reveal well-developed subgrain boundaries (where there is an abrupt change in contrast). There are some dislocations within these subgrains, but also in the nearby surroundings. Examination of this and other scars show that the dislocation density decreases with distance from the subgrain regions (additional images of scars with multiple channeling conditions

are in figures A4–A6 in the appendix). The well-defined subgrains are about  $1\ \mu\text{m}$ , and the KAM and GROD-angle maps in figure 7 show that the subgrains are misoriented from the surrounding material by a few degrees.

Similar ECCI analysis of Sample I in the appendix (figure A4) shows that hydride scars following one MO cryogenic cycle had more randomly distributed dislocations and less distinct subgrain structures than Sample II in figure 6, which had multiple MO cycles and HT. Following HT, sample I showed similar LAGB patterns as in figure 6, with sharp subgrain boundaries and randomly distributed dislocations (figure A5). This suggests that despite the repeated cryogenic and heat treating cycles in Sample II, the dislocation and scar morphology in figure 6 represents the same kinds of defect arrangement that initially developed with the hydride formation during the first MO cryogenic cycle and their recovery after HT.

EBSD analysis of the scar in figure 6 is shown in figure 7. The IQ map shows high IQ in and immediately surrounding the scar and lower IQ in the surrounding regions. The IPF map shows orientation gradients within the scar and white lines marking LAGBs, which are correlated with a higher GND density ( $\rho > 10^{14}\ \text{m}^{-2}$ ), as shown in the GND density map generated by HR-EBSD cross-correlation analysis. The KAM map shows about a  $3^\circ$  misorientation for many of the sub-grain boundaries (LAGBs). Some similarly high misorientations in the regions surrounding the scar are consistent with the dislocation content observed in the ECCI analysis. The subgrain



**Figure 5.** BSE image of the subsurface after 150  $\mu\text{m}$  removal and a specific scar (white arrow, lower inset) examined using ECCI in figure 6 under the channeling condition  $\mathbf{g} = (200)$ . The prism and colored solid and dashed lines in the lower grain represent plane traces to be compared with the scar morphology. The sample and images are rotated counterclockwise about  $25^\circ$  from those in figure 2.

size characterized by the GROD is somewhat larger than that observed by ECCI, due to the  $1^\circ$ – $2^\circ$  misorientation threshold and EBSD resolution limits. There are regions of low KAM within and immediately surrounding the scar, consistent with a locally recovered structure, while a little farther away, GNDs required to accommodate the orientation gradient are present. The GROD-angle map shows a uniform orientation (by uniform yellow-green colors) consistent with the regions of low KAM values (blue) in the interior of subgrains. The GROD-axis map shows mottled regions outside of the scarred regions that reflect the average orientation, and the LAGB regions have varying rotation axes from the average (specific colors) within different subgrains. The hydrides produce significant damage well below the surface, deeper than the 25  $\mu\text{m}$  depth of the surface hydrides in figure A2.

#### 4. Discussion

While it is well-known that removing hydrogen from Nb cavities is critical for good performance, this investigation

revisits the negative effects from forming hydrides in an effort to better understand the source of this damaging behavior. Also considered is the apparent contradiction that the material with hydrides can resist flux penetration by a stronger magnetic field than the same material after HT with recovered hydride scars that contain LAGBs (recognizing that current cavity fabrication paths do not generate hydride scars such as those investigated here). Using the results from MO imaging and hydride scar microstructure analysis using EBSD and ECCI, the two questions proposed in the introduction regarding relationships between hydride formation, residual dislocation structures, GBs, cryo-cooling, HT, and trapped flux are assessed, and new hypotheses are then identified.

##### 4.1. GBs, hydrogen, and flux penetration: do hydrides facilitate GB flux penetration? If so, do GBs favor hydride formation?

**4.1.1. The effect of GB inclination on flux penetration.** Previous study has shown that flux penetration at GBs occurs when

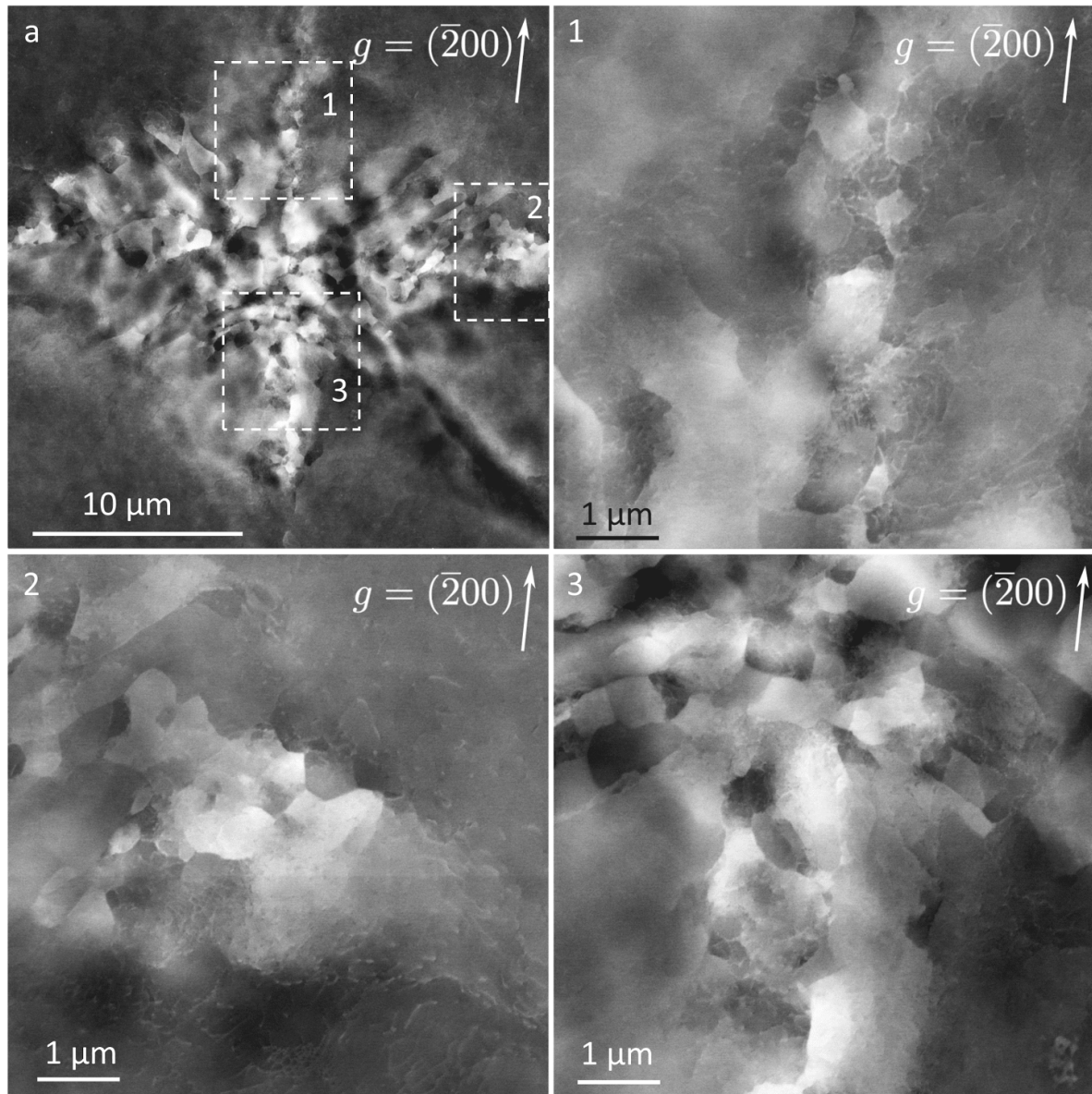


**Figure 6.** Electron channeling contrast image (a) and three ECCI images of the numbered areas in white dashed-line boxes. The sample and images are rotated counterclockwise about  $25^\circ$  from those in figure 2.

the boundary is parallel to the magnetic field [24], which is also confirmed in this study: Sample I with a GB not perpendicular to sample surface did not show GB flux penetration (figure A1), while Samples II and III, with an inclination angle close to 90 degrees from the surface, showed GB flux penetration when the magnetic field was parallel to the HAGB. Flux penetration was also observed along a LAGB in a deformed Nb single crystal described in [19], but its inclination was not known. Flux entered along the HAGB and the LAGB during the first cryo-cooling cycle, as shown in figure 3(i) (and the ZFC image in figure 1), and joined where the LAGB met the HAGB. After removing 180  $\mu\text{m}$ , the flux penetration along the left side of the HAGB did not occur (figure 3(iii)) due to the remaining HAGB being highly inclined to the field. After removing material, the LAGB was still nominally parallel to the field, except where the LAGB joined the HAGB

where it was no longer parallel to the field (figure 4). This also suggests that flux may penetrate as easily along LAGBs as HAGBs despite their difference in structure; LAGBs are composed of organized dislocations while HAGBs consist of polyhedral defect structures.

**4.1.2. The effect of hydrogen on flux penetration.** The MO images show that a preferential GB flux penetration correlates well with a GB transparency significantly less than 1 ( $J_c^{\text{grain}} > J_c^{\text{GB}}$ ), which occurs when hydrides are present. Hydrogen introduced into the Nb surface increases the surface pinning or  $J_c^{\text{grain}}$ , resulting in a different  $J_c$  in the grain and GB regions. After HT, the low hydrogen content implies much less hydride content, and  $J_c^{\text{grain}}$  values are similar to  $J_c^{\text{GB}}$ , leading to reduced surface pinning and no significant difference

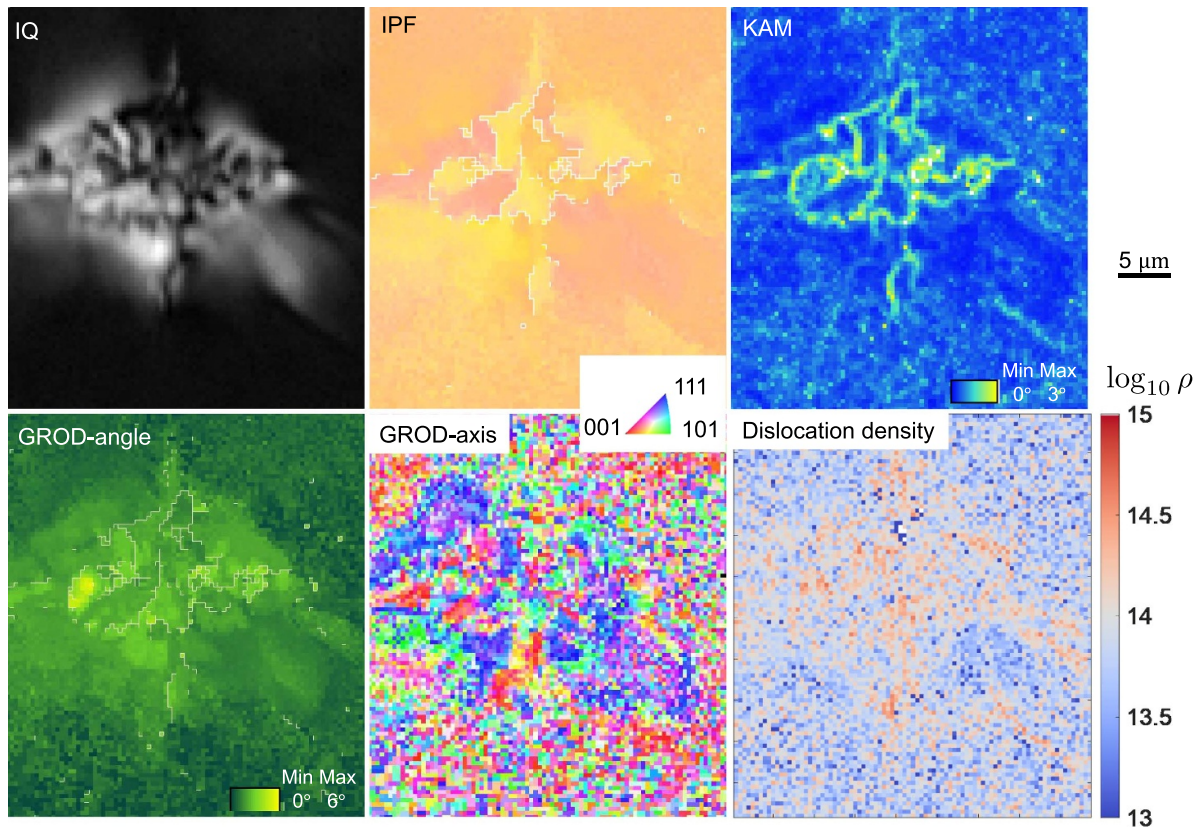


**Figure 7.** IQ, IPF, KAM, GROD-angle, GROD-axis, and GND density maps of the scar shown in figure 6 generated from an EBSD scan with a step size of  $0.4 \mu\text{m}$ . LAGBs are marked using white lines in the IPF, and GROD-angle maps. The dislocation density map shows higher GND densities ( $\text{m}^{-2}$ ) near the LAGBs.

in superconducting behavior between the grain and the GB (figure 3(ii)). The superconducting penetration depth in Nb is of the order of 40 nm, and GBs are not expected to alter the superconducting properties of clean Nb. A similar result of higher  $J_c^{\text{grain}}$  as a consequence of introducing hydrogen by polishing was observed in the case of a RRR 300 Nb sample with a LAGB, which showed preferential GB flux penetration in the presence of surface hydrides [54].

These observations show the critical role that hydrogen plays in flux pinning in the presence of GBs. The above observations do not prove that the GB structure itself is directly responsible for the higher GB flux penetration, but they can synergistically cause flux penetration with the presence of hydrogen. While annealing reduces the potential to form hydrides, the fact that flux penetration occurs when a particular current density is reached that is correlated to prior damage in the GB suggests that hydrides in the bulk are less damaging than in the GB, and that damage caused by hydrides in the boundaries compromises the niobium irreversibly.

**4.1.3. Flux penetration along GBs.** GBs are segregation sites for impurities, including hydrogen. The fact that the first MO image (figure 1(b)) shows premature flux penetration along the boundaries suggests that the boundaries may

favor the formation of hydrides and hence, enable flux penetration. Sung *et al* [19] observed flux penetration along LAGBs in a deformed single crystal that exhibited hydride formation along the boundary (at about 500–600 Oe at 7–8 K) while other LAGBs did not trap flux. These LAGBs had hydride scars decorating the LAGB with a precipitate free zone near the LAGB (indicating that the LAGB was a trap or sink for hydrogen). In the current study, where the material was not deformed, flux penetration was observed along a LAGB where there were no obvious hydrides (the obvious hydrides appear to be correlated with surface scratches). Flux can be trapped in defect structures that are larger than the coherence length of superconducting electrons (about 40 nm [20]). It is not clear if the flux penetration was due to the hydrides, dislocations generated by forming the hydrides, or pre-existing dislocation accumulation from deformation in the vicinity of the boundary, or inherent to the low angle boundary structure.

**4.1.4. Bulk flux penetration and trapping caused by hydrides nucleated in the LAGB.** The FC mode MO image in figure 1(f) with a field twice as large as needed to cause trapped flux in the GBs indicates that bulk flux trapping in Nb can occur with a high enough field. Based upon microscopy in figures 6–8, hydride damage is also present  $150 \mu\text{m}$  below a

surface exposed to hydrogen via polishing, though these subsurface hydride scars are smaller than scars on the original surface. However, scars are usually larger and more prevalent at the GB. Surprisingly, the scars are deeper in the bi-crystal than in the single crystal shown in appendix figure A2, which are only about 20–50  $\mu\text{m}$  deep. Without prior deformation or LAGBs, the lower number of defects that enable transport and/or concentration of subsurface hydrogen may prevent the formation of large hydrides within the bulk crystal, and favor formation in a LAGB. Recent results also confirm that the LAGB and very fine grains with limited grain growth lead to early flux penetration [55, 56]. Nevertheless, the fact that bulk flux penetration occurs at lower fields following annealing suggests that residual dislocations surrounding scars and LAGBs within scars may facilitate bulk flux penetration more easily than when hydrides are present, suggesting that hydride scar dislocation substructure may facilitate trapped flux more effectively than hydrides. It is possible that local hydrostatic tensile strains resulting from dissolution of hydrides (see figure 5 in [26]) may generate more dislocation substructure upon reheating (by recovery into LAGBs) than is present when hydrides are present.

**4.2. Dislocations, hydride formation, and flux penetration: does hydride formation cause multiplication of dislocations, which provide sites for subsequent hydride formation and flux penetration?**

**4.2.1. Hydride formation causes dislocation generation.** Large hydride scars ( $\sim 50 \mu\text{m}$ ) on the original surface were observed along both the HAGB (KAM map in figure 4) and residual polishing scratches/scratch paths (figure 2) after the first MO experiment, but not along the LAGBs. Both GBs and high dislocation density regions beneath scratches [56] can attract hydrogen atoms that form Cottrell clouds [57] and facilitate hydride formation. The hydride scars observed after chemical removal of 150  $\mu\text{m}$  are smaller, indicating that the hydrogen concentration decreases with depth into the bulk Nb<sup>3</sup>. The dislocation structures in and near hydrides experienced recovery after HT, leading to sub-grain formation within the scars, as shown in ECCI images (figure 6 and appendix figure A4). A high dislocation density provides a large recovery driving force, which could explain the well-defined sub-grains and higher EBSP IQ within the scars and the lower IQ in the surrounding areas.

**4.2.2. Dislocation networks, in turn, are preferred sites for hydride re-formation.** Despite the large number of hydride scars associated with surface scratches, there is no correlation between flux penetration and the distribution of these surface hydride scars. In contrast, flux penetration shown in figure 3 indicates that trapped magnetic flux occurred along the LAGB, and HAGBs parallel to the field. Removal of the hydride scars

on the surface did not change flux pinning along the LAGB in subsequent cryo cycles, so flux pinning at this LAGB is not affected by surface hydrides. This suggests that subsurface hydrides are more important.

Prior observations in Nb samples at higher temperature and higher hydrogen concentration indicated that hydrides form preferentially where they had been present in the past. Using *in-situ* TEM, Schober directly observed hydride re-precipitation at locations where hydrides had previously formed during temperature cycling [33]. Also, Makenas and Birnbaum [29] observed a large hydride that nucleated on a LAGB during *in-situ* cooling to 77 K of a hydrogen charged TEM foil. As the stochastic nature of dislocation glide and cross-slip is not reversible, it is likely that the dislocation density in these scars will increase with each cryogenic cycle if hydrogen is present. As the critical current in GB regions did not change much after HT (figure 3), this suggests that damage in and near boundaries was not healed, and that degradation of superconducting behavior could occur with each cryo cycle. The ECCI images in figure 6 show high dislocation density in and around the hydride scar after four MO cooling cycles and two HTs. Hence, repeated cryogenic cycles would be expected to result in locally complex repetitions of dislocation generation from formation and dissolution of hydrides.

In the present study, it is clear that hydrides formed at both the LAGBs and HAGBs (figures 2 and 5). In the subsurface volume, hydride scars are especially visible in the KAM map in figure 4, which are smaller but more densely distributed along part of the HAGB, but the scars are larger and more scattered along the LAGBs near the HAGB, as well as some distance from the HAGB. The smaller size of hydrides adjacent to HAGBs suggests that nucleation may be easier in the HAGB, perhaps due to a higher density of stored hydrogen in the defect structure, but growth is faster in the LAGB. Faster growth in the LAGB will more quickly lead to plastic accommodation and generation of dislocations. The larger hydrides in the LAGB may also be an important factor for pinning flux, as it is clear in figures 3(i) and (iii) that the flux penetration develops easily along the entire LAGB, but flux penetration did not occur along the entire HAGB. Interestingly, the scattered smaller hydrides throughout the grain interior do not appear to be strongly associated with preferential flux pinning, perhaps due to lower overall hydrogen concentration and smaller sizes than on the LAGB (figure 5, and uniformly distributed in deformed single crystals in [19]).

One possible explanation for preferred hydride growth at LAGBs is that when hydrides form at these boundaries, they develop semi-coherent interfaces on both sides of the hydrides and grow to  $\sim 30\text{--}40 \mu\text{m}$ . In contrast, due to the larger mis-orientation across the boundary, HAGB hydrides could be semi-coherent on only one side of the hydride, and the higher energy HAGB interface leads to easier nucleation conditions that may account for them being only 1–5  $\mu\text{m}$ . Hydrides in the grain interior range from 5–30  $\mu\text{m}$ . These conditions would be expected to differ in deformed material, which would contain a larger dislocation density. This is consistent with the well-known (if poorly documented) phenomenon that cavity efficiency tends to drop in deformed cavities [58].

<sup>3</sup> The 3D constraint (lack of a free surface) may also account for smaller subsurface hydrides in Sample I and Sample II after surface removal, than on the original free surface of Sample II.

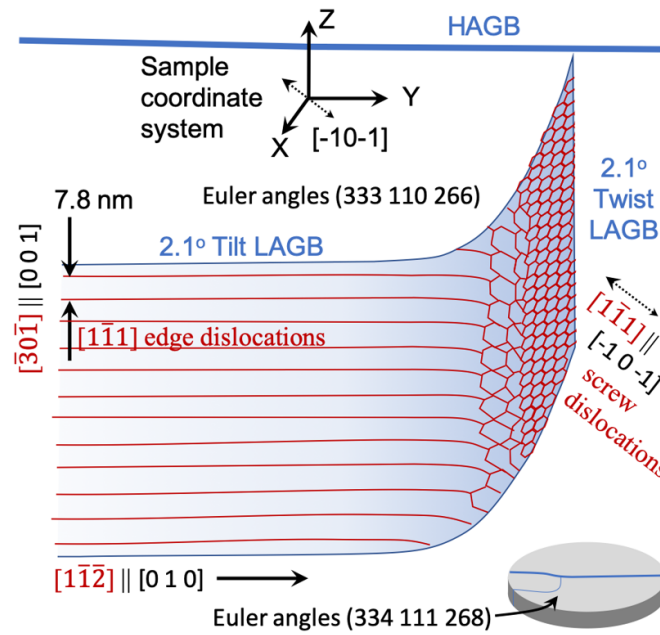


**Figure 8.** Depiction of dislocation arrangement in the LAGB that traps magnetic flux. Crystal directions are in red, sample X-Y-Z coordinate system is shown in black.

**4.2.3. Dislocation spacing in LABGs and recovered hydride scars.** Examination of the misorientation across the subgrain displaying the flux penetration shows that the boundary is misoriented  $\sim 2.1^\circ$  (based on EBSD measurements) about a crystal axis of  $[1 \ -1 \ -1.73]$  in the enclosed subgrain, which is close to the  $[1 \ -1 \ -2]$  axis. Expressed in the sample coordinate system, this as-measured rotation axis lies close to the sample Y-axis ( $[-0.031 \ 0.992 \ -0.126]$ ) as shown in figure 8. With this rotation axis, the portion of the LAGB close to the HAGB (i.e. the segment nearly perpendicular to the Y-axis) must be a twist boundary, which requires at least two sets of screw dislocations with different Burgers vectors (for example, see [59]), while the portion of the LAGB further from the HAGB (and close to parallel to the HAGB) is a tilt boundary, roughly parallel to the Y-axis. Tilt boundaries are made up of one or more types of edge dislocations, but they will all have the same line directions, parallel to the tilt axis. In this tilt boundary section, the dislocations are arranged parallel to the boundary and roughly parallel to the surface, i.e. perpendicular to the crystal surface normal of  $[-3 \ 0 \ -1]$ . For tilt boundaries, the spacing  $s$  of dislocations is a function of the misorientation angle  $\theta$  (in radians), given by

$$s = \frac{b}{\theta} \quad (3)$$

where  $b$  is the magnitude of the Burgers vector. Edge dislocations with a  $[1 \ -1 \ -2]$  rotation axis have a Burgers vector  $\mathbf{b} = 1/2[1 \ -1 \ 1]$ , with a magnitude of 0.286 nm. Consequently, with this  $2.1^\circ$  misorientation, the dislocations are spaced about 7.8 nm apart in the tilt boundary in the through-thickness direction, as depicted in figure 8. As Nb is BCC, it is expected that the twist portion of the boundary will be made up of three different  $1/2 \langle 111 \rangle$  dislocations [59] with similar spacing to

the dislocations in the tilt portion of the boundary. The spacing of these dislocations in the Z-direction will likewise be similar to that of the tilt boundary, but more critically, will also be significantly smaller than the  $\sim 40$  nm coherence length. Furthermore, the LABGs resulting from HT of hydride scars cause LABGs with similar misorientations, and hence, similar dislocation spacings, so if a low angle boundary with hydrides can trap flux, then recovered hydrides scars may also be able to trap flux.

This work shows that if the hydrogen is eliminated from the material using vacuum HT (which generates LABGs in hydride scars) the flux pinning is quite uniformly distributed across the material, as evident in figures 3(ii) and (iv), and flux penetrates at a significantly lower field, possibly due to the widely distributed residual hydride scars containing LABGs. While both the LABG and the HAGB showed very strong flux pinning in the presence of non-superconducting hydrides, it occurred at significantly higher magnetic fields. Surrounding the hydrides, there is no recovered LABG structure, such that the only LABG substructure in the material would be in LABGs parallel to the field where hydrides are *not* present.

Clearly, the hydrides themselves play a critical role in superconducting performance, as they interfere with the path of superconducting electrons, but perhaps they are an indirect cause of flux pinning. It is difficult to imagine how to disentangle the interactions of hydrides, hydride scars, LABGs and HAGBs under superconducting/flux pinning conditions. Thus, the specific underlying mechanisms for the flux pinning at GBs is difficult to state with certainty. However, recent systematic studies do indicate that a grain size or GB density relationship with flux penetration behavior exists. These studies show that flux penetration and expulsion is easier in large grains resulting from grain growth to a size greater

than 100  $\mu\text{m}$  that may sweep out LAGBs, whereas penetrating flux gets trapped when the grain sizes are of a finer dimension of  $\sim 30\text{--}50\ \mu\text{m}$  [55], in which the likelihood of GB facets being aligned with the magnetic field would be larger.

**4.2.4. Overall assessment and new hypotheses.** Overall, the relationships between hydrides, dislocation networks, and flux pinning are complicated and may (still) be inseparable [60]. Advanced flux characterization methods with micrometer to nanometer level resolution would enable further exploration of the influence of dislocations, hydrides, and the related hydride [61] scars. Hence, hypotheses developed from this study regarding the interrelationship between hydrogen, dislocations, and flux trapping are provided to guide future work:

- The small (<10 nm) dislocation spacing in LAGBs may facilitate flux pinning [43].
- Hydrides may not cause flux pinning but the dislocations generated by them and the reverse strain from their dissolution result in high dislocation density that can recover into LAGB networks with a HT.
- While HAGBs may hold more hydrogen and nucleate hydrides more easily than LAGBs due to their more open structure, large hydrides may grow more easily at LAGBs, facilitated by a lower interfacial energy and rapid hydrogen transport from HAGBs via the dislocations comprising LAGBs.
- Uniformly distributed damage caused by bulk hydride precipitation facilitates bulk flux penetration due to formation of LAGB networks within hydride scars during HT, resulting in degradation of superconductivity that would decrease cavity performance.
- Once hydride scars are present, they can only be removed by a HT that causes motion of HAGBs (recrystallization/grain growth).
- Hydrides may inhibit easy flux penetration flow as they are insulating.

Clearly, further study is necessary to determine if these hypotheses are correct and underpin general mechanistic behavior. If so, this implies that recrystallization of cavities following forming in order to remove LAGBs is desirable to reduce trapped flux.

## 5. Conclusions

MO imaging results from one bi-crystal sample with both a HAGB and a LAGB parallel to the magnetic field show flux penetration associated with the position of the boundaries. Flux penetration patterns are susceptible to hydrogen contamination from the surface, which can be manipulated through heat and surface treatment. This preferential flux penetration can be turned on or off by introducing hydrogen and removing

hydrogen by HT. Larger hydrides (and hence, more dislocation generation) form in low angle than HAGBs.

ECCI observations reveal that hydride formation during cooling and subsequent reheating and dissolution causes significant local dislocation multiplication, the networks of which could in turn provide favored sites for hydride reformation during subsequent MO cooling cycles. The relationship between hydrides, dislocation networks, and flux pinning is complicated and difficult to disentangle. The fact that the sample shows bulk flux trapping in field cooled MO images indicates that the bulk flux penetration was changed due to the damage caused by hydride precipitation.

Nb is susceptible to hydrogen loading during polishing or chemical milling, which leads to a high hydrogen content that forms hydrides during cooldown. Hydride formation creates significant surface deformation of the Nb, and the damage extends beyond tens of microns below the surface. The plastic deformation created by the hydrides is not reversible with an 800 °C HT. This work suggests that the formation of LAGBs during Nb cavity manufacturing and surface preparation should be minimized and reinforces that hydrogen contamination causes damage and that this damage cannot be easily healed.

## Data availability statement

The data that support the findings of this study are available upon reasonable request from the authors.

## Acknowledgments

The authors thank Pashupati Dhakal from Jefferson Lab for performing heat treatments and nitrogen infusion on the samples. TRB and MW acknowledge support of the Department of Energy Award DE-SC0009962. SB, SC, AP, and PJJ acknowledge Award DE-SC0009960 and the State of Florida. The National High Magnetic Field Laboratory is supported by National Science Foundation Cooperative Agreement Nos. DMR-1157490 (-2017) DMR-1644779 (2018-) and the State of Florida.

## Appendix

This appendix presents information about measurements on samples I and III that provide helpful context for the main paper. Table A1 provides details for all three samples to facilitate comparison. The inclination angle of the GB is defined as the angle between the GB plane and the sample surface. In Sample I the GB inclination angle was uniformly 80°, in Sample II it varied from 90° (in the right 2/3 of the boundary) to about 82° (in the left 1/3 of the boundary), and in Sample III the GB is twisted, with an inclination angle that varied from 84°–90°. The final thickness of the three samples after vibratory polishing and a light BCP and before MO observations is listed in table A1.

**Table A1.** Sample size before MO imaging and GB characteristics.

Sample	I	II	III
Diameter (mm)	2.86	2.84	2.89
Thickness (mm)	1.00	0.79	0.9
Misorientation (°)	53	24	11
Inclination (°)	80	82–90	84–90 (twisted)

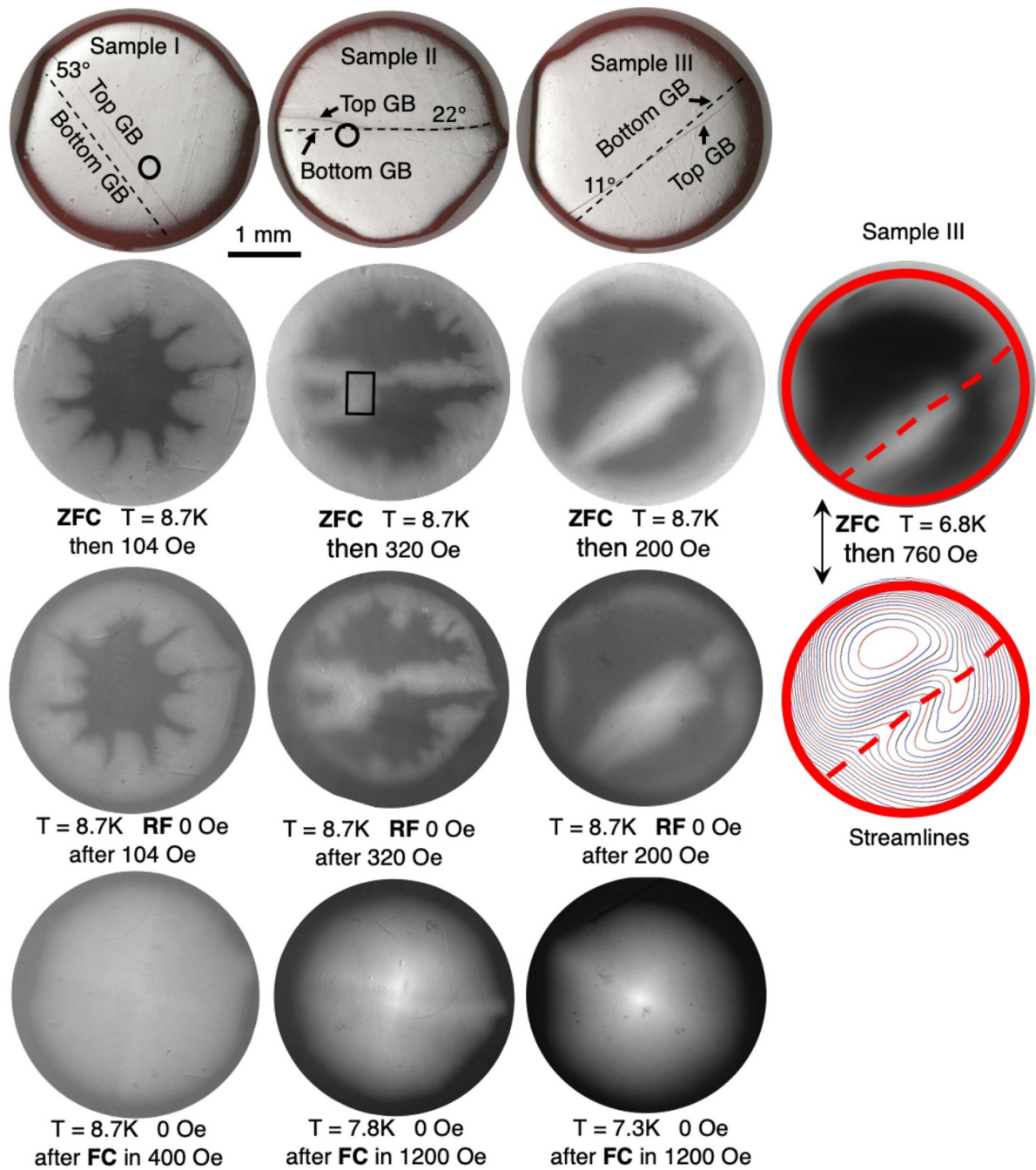


**Figure A1.** Surface optical images (row 1) showing location of GBs on the top and the bottom surfaces (dashed line) and MO images in ZFC, RF, and FC modes with values of temperature (T) and applied magnetic field (H) indicated (rows 2–4). The black circles indicate locations where ECCI imaging was performed. The black rectangular outline indicates the area examined using EBSD, as presented in figure 2. An extra ZFC image and the corresponding streamline map is shown for Sample III.

**Table A2.** Summary of Magneto Optical imaging results at different stages of cryo-cycle and HT history of all three samples.

History	Sample I (tilted GB)	Sample II ('fork')	Sample III (twisted GB)
1st MO (cryo-cycle)	No preferential GB flux penetration; finger-like flux penetration from edge ZFC 8.7 K, 104 Oe	LA, HA GB flux penetration ZFC 8.7 K, 320 Oe, repeated at 7.8 K, 560 Oe, slightly less penetration	Partial GB penetration ZFC 8.7 K, 168 Oe in GB oriented    field
Surface SEM after 1st MO	Numerous hydride scars (~50 $\mu\text{m}$ )	Numerous hydride scars (~50 $\mu\text{m}$ )	Numerous hydride scars (~50 $\mu\text{m}$ )
2nd MO after 800 °C HT + N <sub>2</sub> infusion (H removed)	N/A	Fork flux penetration not observed; uniform penetration from edge at lower field (ZFC 6.4 K, 220 Oe)	N/A
3rd MO after mechanical polishing (H reintroduced)	N/A	Fork flux penetration restored (ZFC 7.8 K, 440 Oe)	N/A
1st ECCI after 150 $\mu\text{m}$ BCP	Small hydride scars (~3 $\mu\text{m}$ ); high density dislocations in scars, no LAGB (figures A3 and A4)	Smaller scars (~20 $\mu\text{m}$ ); high density dislocations + many LAGBs in and near scar (recovery)	N/A
2nd ECCI after HT and N <sub>2</sub> , 30 $\mu\text{m}$ BCP	LAGBs and dislocations observed in scar (recovery) (figures A5 and A6)	N/A	N/A

### • MO results of all three samples

MO results are shown in figure A1 to enable comparison. Sample I was cooled to 8.7 K in a zero-field mode (ZFC), followed by application of an external field of 104 Oe. The ZFC image in figure A1 shows flux penetration from the sample edge as a bright ring, wherein no flux penetration was observed along the GB with a 80° inclination angle from the surface. After that, the external field was removed (next MO image) to collect the RF image, which shows trapped flux as bright contrast. In order to obtain the FC image, the sample was reheated above 9.3 K with no field applied, and then FC in an external field of 400 Oe, followed by the removal of this field after the temperature reached 8.7 K, when the FC image showed uniform bulk flux trapping (bright contrast).

In sample III, a similar MO imaging and cooling history was used: the ZFC imaging shows preferential GB magnetic flux penetration at 8.7 K after application of 200 Oe despite the GB being tilted near the sample edges, where the GB is a few degrees from parallel to the field. The middle part of the GB is nearly parallel to the magnetic field and admits flux. The RF image taken after the field was reduced to zero from 200 Oe shows trapped flux along the GB with different amounts of trapped flux in the two segments of the boundary. The FC image shows the trapped flux in the bulk, with no apparent GB effect. The fourth column shows a MO image of Sample III at a lower temperature and a high field with a similar flux penetration pattern. The corresponding current streamlines clearly show that the GB causes distortion to superconducting current, which is curved along the GB.

Tables A2 and A3 compare the thermal cycling and HT history of the three specimens, and how the MO imaging

compares with other characterized grain and sub-grain boundaries in prior work [19, 24].

### • Hydride scars

SEM images of hydride scars are shown in figure A2 on a single crystal niobium sample after MP and a MO cryogenic cycle. MP loads the Nb surface with hydrogen, and residual dislocations resulting from coarser grit grinding may be present beneath the surface. The top view (b) shows hydrides with dendritic growth directions that vary, depending on the grain orientations. Hydrides are formed on the sample surface during cooling and extend into the Nb surface anywhere between 20 and 30  $\mu\text{m}$ , especially along sub-grain boundaries, as indicated by the BSE contrast (c), indicating local rotations caused by plastic deformation during hydride formation.

### • ECCI and EBSD analysis of hydride scars in Sample I

Sample I was examined twice using ECCI, first after hydride scars were formed from the MO experiment (cryogenic cycle), then after the HT. The surface quality of Sample I after its first MO cryogenic cycle was not sufficient for ECCI, so BCP was used to remove 100–150  $\mu\text{m}$  from the surface and still preserve sample flatness for ECCI observations. Despite removal of more than 100  $\mu\text{m}$ , the subsurface of Sample I was still covered with a large number of hydride scars, as shown in the BSE image in figure A3, but they are about 3  $\mu\text{m}$  in size, ~6% of the size of the ~50  $\mu\text{m}$  scars observed in sample II in figure 2 before the surface was removed. The EBSD maps show a lower IQ at scars, indicating a higher defect content.

**Table A3.** Comparison of MO imaging conditions with previous work [1, 2].

Sample	GB surface inclination	Misorientation	MO results	T and H
I	$\sim 80^\circ$	$53^\circ$	Finger-like flux penetration from edge	8.7 K, 104 Oe
II	$\sim 90^\circ$	HAGB, $22^\circ$ LAGB, $2^\circ\text{--}3^\circ$	HA and LA GB flux penetration Mostly LAGB flux penetration	8.7 K, 320 Oe 7.8 K, 440 Oe (HT + MP)
III	Twist that includes $\sim 90^\circ$	$11^\circ$	Flux penetration where GB is parallel to field	8.7 K, 200 Oe
b* [19]	Single crystal Inclination unknown	LAGB $\sim 0.5^\circ$	LAGB flux penetration	7 K, 600 Oe 7.2 K, 400 Oe (HT)
d* [19]	Single crystal Inclination unknown	LAGB $\sim 0.5^\circ$	LAGB flux penetration	8.2 K, 520 Oe 7.2 K, 356 Oe (HT)
B* [24]	Bicrystal Inclination $\sim 90^\circ$	$36^\circ$	HAGB flux penetration	6 K, 320 Oe
D* [24]	Bicrystal Inclination $\sim 90^\circ$	$17^\circ$	HAGB flux penetration	6 K, 800 Oe

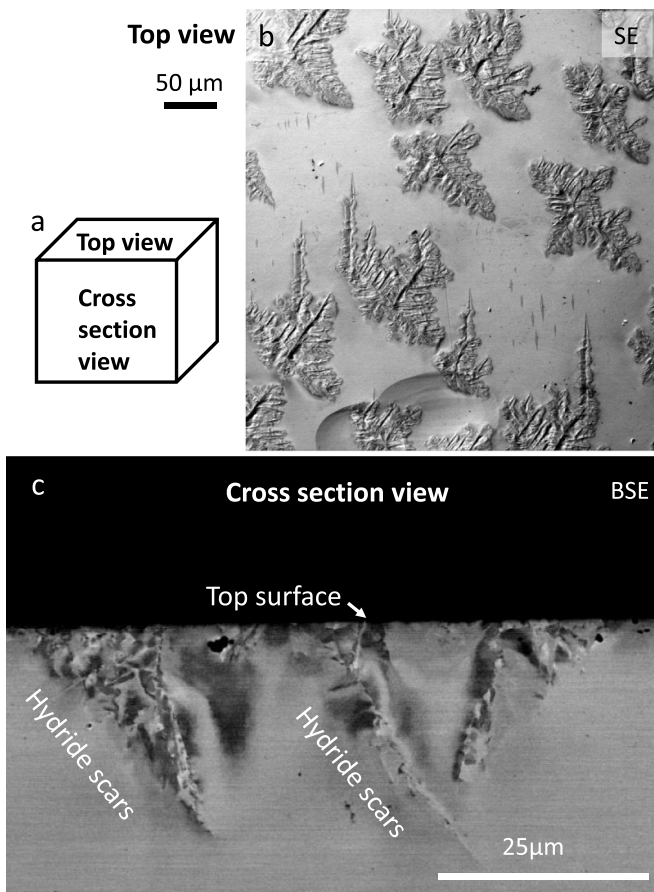


**Figure A2.** Top view (b) and cross section view (c) images of a mechanically polished Nb single crystal sample after a cryogenic cooling cycle. The surface scars are about five times as broad as they are deep.

The KAM map shows that the scar caused about a  $3^\circ$  misorientation, consistent with the hydride scars observed in Sample II (figure 2).

ECC images of the scar indicated by the red arrow in figure A3 are shown in figure A4 under two different

channeling conditions. With  $\mathbf{g} = (00\bar{2})$ , the density of individual dislocations increases toward the center of the scar, where it is difficult to resolve individual dislocations. There are regions with bright or dark contrast inversions in the middle of the scar, suggesting subgrain formation. In some areas around the scar, there is evidence of dislocation pile-ups (red arrows). This is consistent with the plastic deformation required by the hydride precipitation and dissolution. Multiple slip systems appear to have been activated; dislocation B is visible for both imaging conditions, while dislocation A with a 'V' shape is only visible for  $\mathbf{g} = (00\bar{2})$ , indicating that A and B have different Burgers vectors. It is known that the dislocations move out from the center during hydride formation but experience reverse motion during hydride dissolution [30, 32]. The plastic deformation is not expected to be completely reversible, as the dislocations on multiple systems will interact and entangle, resulting in local work hardening; many of the GNDs are required to preserve the local orientation gradient.

In order to evaluate the effect of HT on the evolution of dislocation structures of the hydride scars in sample I, an  $800^\circ\text{C}$  3-hour HT was carried out followed by a brief BCP etch (removing  $30\ \mu\text{m}$ ) to improve the surface quality. The ECCI images of a representative scar (figure A5) show fewer dislocations in the middle of the scar and well-defined subgrains of  $\sim 1\ \mu\text{m}$ , indicated by abrupt changes in contrast with different contrast arising from different channeling conditions. These boundaries are much sharper and more distinct than before the HT in figure A4, indicating that dislocation recovery occurred during the HT. As in figure A4, dislocation images based upon different  $\mathbf{g}$  vectors indicate that there are a variety of dislocations on different slip systems (e.g. dislocation *i* is visible for both imaging conditions in figures A5(a) and (b), while *iii* is invisible in figure A5(b)). Though significant recovery occurred within the scar during the HT, when hydrogen was expelled from the material, there is a generally lower dislocation density but some dislocation pile-ups (red arrows) surrounding the scar. The KAM plot in figure A6 of a different scar shows a low value in the center, and higher values

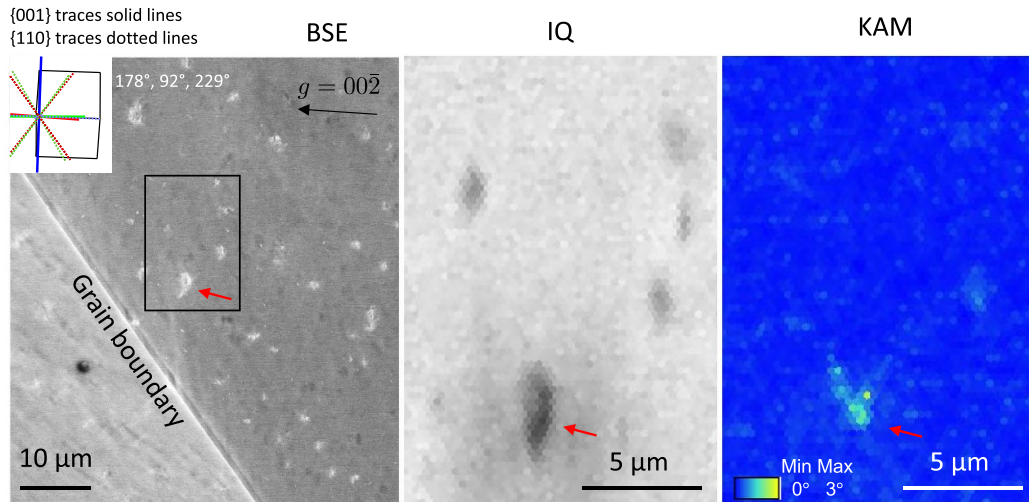


**Figure A3.** BSE image and EBSD scan of sample I before HT; the BSE image shows subsurface hydride scars after removal of  $\sim 100\text{--}150\ \mu\text{m}$  from the surface, the IQ map shows the low IQ scar (red arrow) examined using ECCI in figure A4, and the KAM map shows about a  $3^\circ$  misorientation of the same scar. The location of this region is indicated by a black circle in figure A1 Sample I.

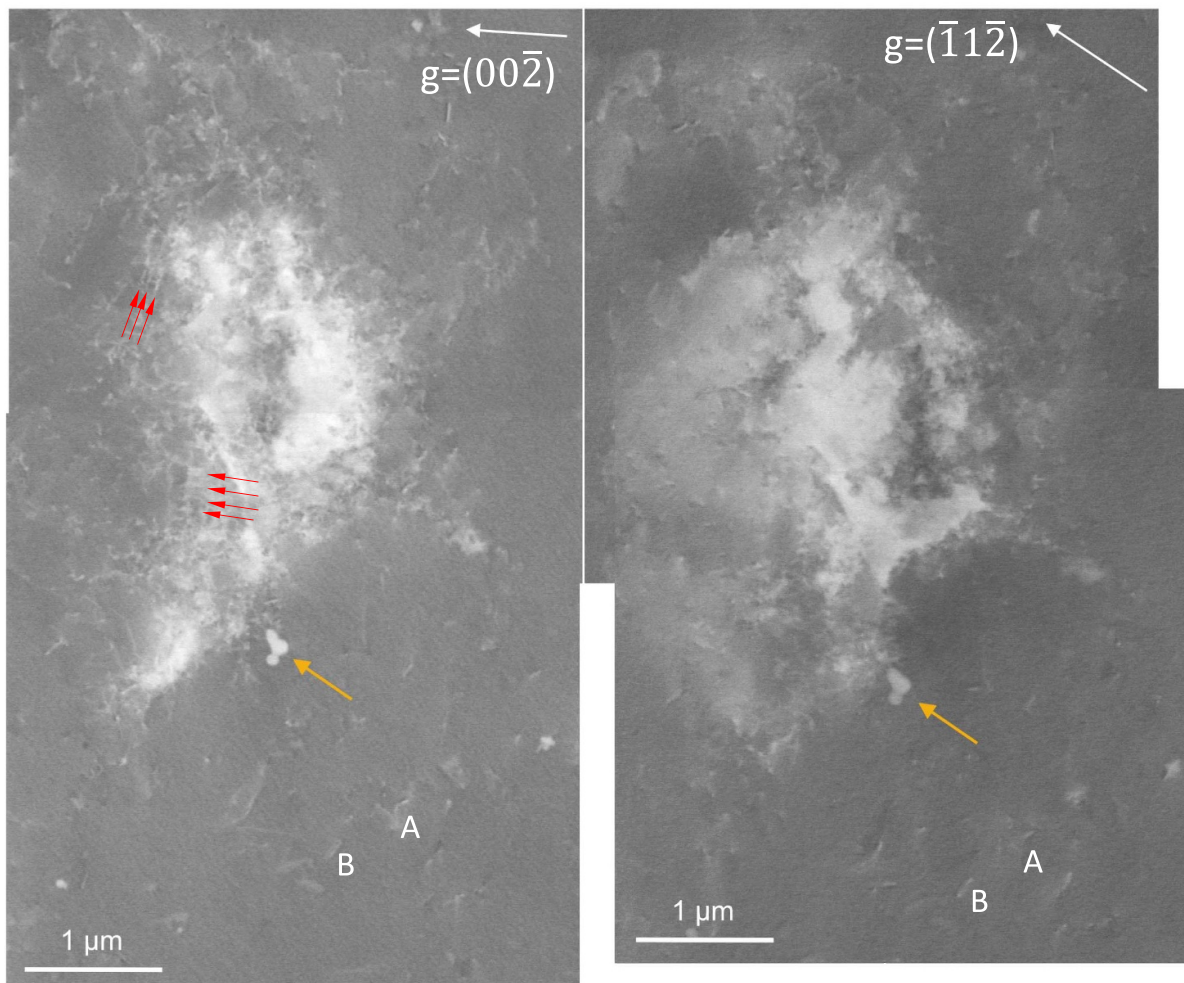


**Figure A4.** Sample I ECCI images under two different channeling conditions ( $g$  vectors represented by white arrows) of a scar on the surface of sample I after MO, before HT. The orange arrow indicates a dust particle used as a landmark.

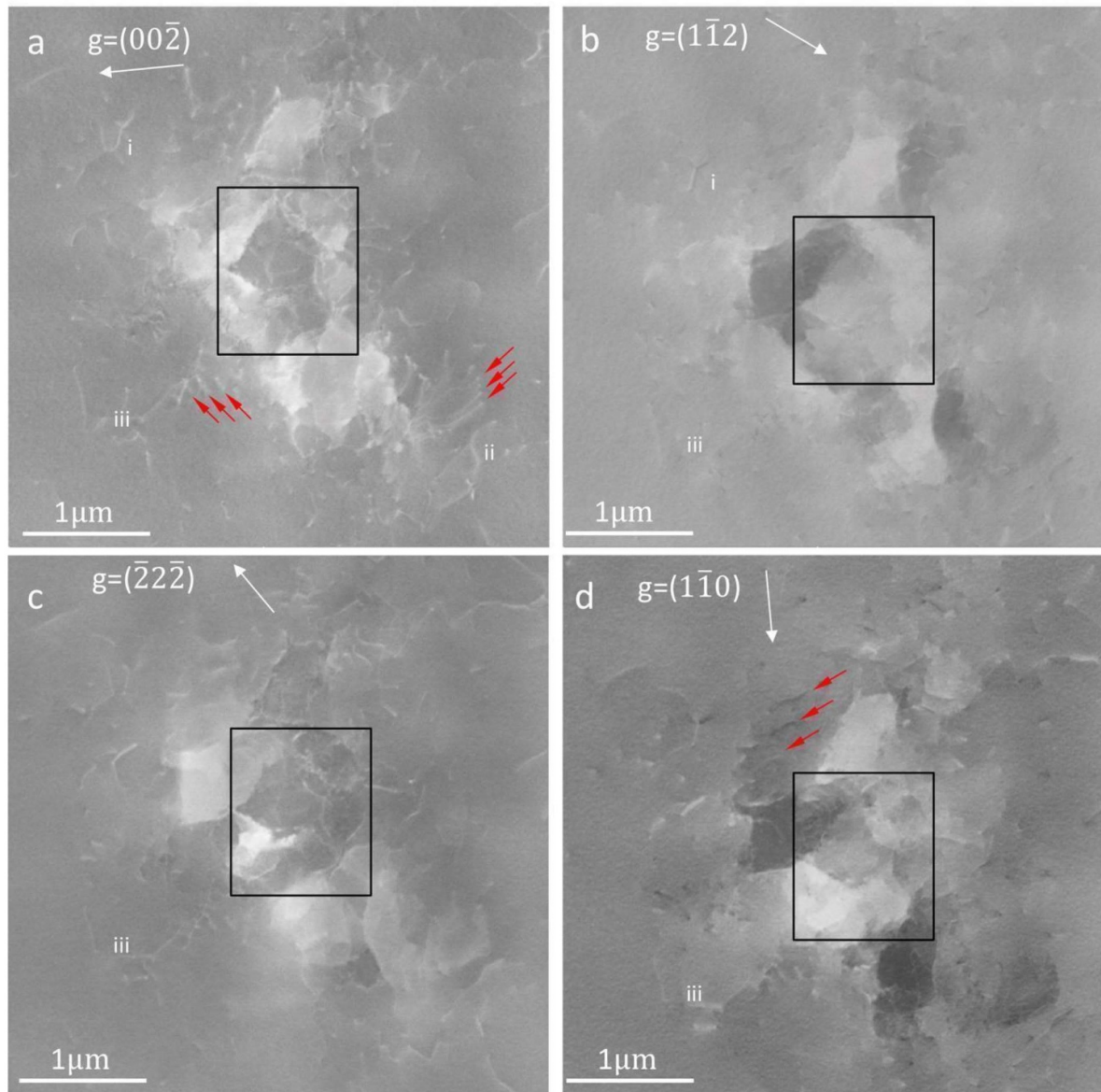


**Figure A5.** Sample I ECCI images of a specific scar after 800 °C 3-hour HT under four different channeling conditions ( $g$  vectors) show development of sub-grains with apparently fewer dislocations. The black box located at the same place in each image enables seeing most of the same LAGBs in the same places.

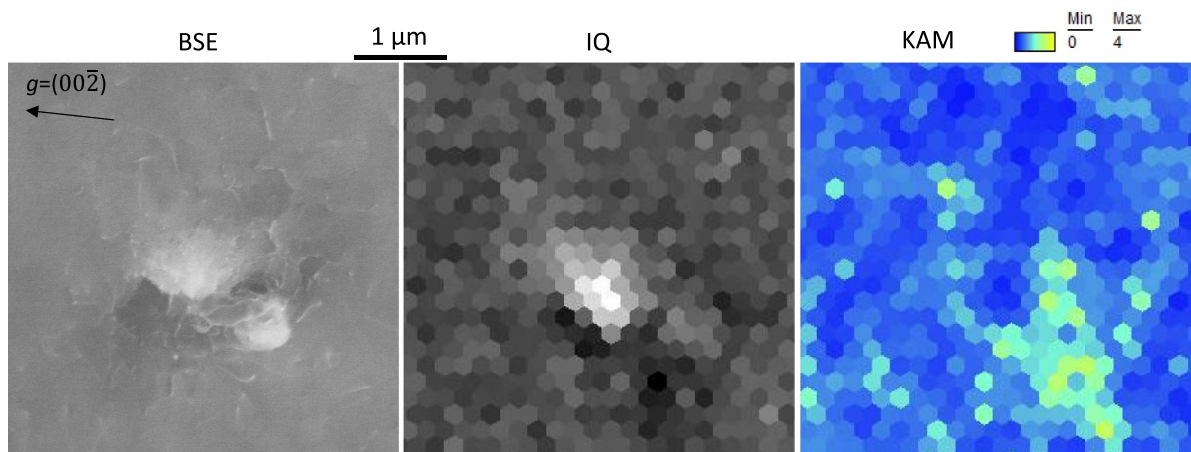


**Figure A6.** Sample I ECCI image and EBSD maps of another hydride scar on the same surface as in figure A5 after 800 °C 3-hour HT. The region of high IQ within the scar corresponds with low KAM, indicating extensive recovery within the scar, but not in the surrounding area.

immediately surrounding it, indicating retention of GNDs surrounding the scar.

## References

- [19] Z.-H. Sung *et al.*, ‘Development of low angle grain boundaries in lightly deformed superconducting niobium and their influence on hydride distribution and flux perturbation,’ *J. Appl. Phys.*, vol. 121, no. 19, p. 193903, 2017.
- [24] A. A. Polyanskii *et al.*, ‘Magneto-optical study high-purity niobium for superconducting RF application,’ in *AIP Conference Proceedings-American Institute of Physics*, 2011, vol. 1352, no. 1, pp. 186–202.
- [30] H. K. Birnbaum, M. L. Grossbeck, and M. Amano, ‘Hydride precipitation in Nb and some properties of NbH,’ *J. Less Common Met.*, vol. 49, pp. 357–370, 1976.
- [32] T. Schober, ‘The niobium-hydrogen system—an electron microscope study. I. Room temperature results,’ *Phys. Status Solidi*, vol. 29, no. 2, pp. 395–406, 1975.

## ORCID iDs

- Mingmin Wang  <https://orcid.org/0000-0002-9284-845X>
- Anatolii Polyanskii  <https://orcid.org/0000-0002-5977-5324>
- Shreyas Balachandran  <https://orcid.org/0000-0002-0077-8504>
- Peter J Lee  <https://orcid.org/0000-0002-8849-8995>
- Thomas R Bieler  <https://orcid.org/0000-0003-0108-8000>

## References

- [1] Singer W 2015 SRF cavity fabrication and materials pp 171–207 (arXiv:1501.07142)
- [2] Padamsee H S 2014 Superconducting radio-frequency cavities *Annu. Rev. Nucl. Part. Sci.* **64** 175–96
- [3] Furuta F *et al* 2006 Experimental comparison at KEK of high gradient performance of different single cell superconducting cavity designs *Proc. 10th European Particle Accelerator Conf. (EPAC'06)* MOPLS084
- [4] Romanenko A, Grassellino A, Crawford A C, Sergatskov D A and Melnychuk O 2014 Ultra-high quality factors in superconducting niobium cavities in ambient magnetic fields up to 190 mG *Appl. Phys. Lett.* **105** 234103
- [5] Williams I and Catterall J A 1966 Effect of heat treatment on the superconducting properties of cold-worked niobium *Br. J. Appl. Phys.* **17** 505
- [6] Bieler T R *et al* 2010 Physical and mechanical metallurgy of high purity Nb for accelerator cavities *Phys. Rev. Spec. Top.—Accel. Beams* **13** 31002
- [7] Ciovati G and Gurevich A 2007 Measurement of RF losses due to trapped flux in a large grain niobium cavity *13th Int. Workshop on RF Superconductivity* pp 132–6
- [8] Checchin M, Martinello M, Grassellino A, Romanenko A and Zasadzinski J F 2017 Electron mean free path dependence of the vortex surface impedance *Supercond. Sci. Technol.* **30** 34003
- [9] Martinello M, Grassellino A, Checchin M, Romanenko A, Melnychuk O, Sergatskov D A, Posen S and Zasadzinski J F 2016 Effect of interstitial impurities on the field dependent microwave surface resistance of niobium *Appl. Phys. Lett.* **109** 62601
- [10] Posen S, Grassellino A, Romanenko A and Melnychuk O 2015 Flux expulsion variation in SRF cavities *17th Int. Conf. on RF Superconductivity* pp 404–8
- [11] Wang M, Kang D and Bieler T R 2018 Direct observation of dislocation structure evolution in SRF cavity niobium using electron channeling contrast imaging *J. Appl. Phys.* **124** 155105
- [12] Aull S, Kugeler O and Knobloch J 2011 Study of trapped magnetic flux in superconducting niobium samples *SRF2011 15th Int. Conf. on RF Superconductivity (Chicago, IL USA)* THPO006
- [13] Wang M, Bieler T R, Compton C and Kang D 2018 Characterization of microstructural defects in SRF cavity niobium using electron channeling contrast imaging *18th Int. Conf. on RF Superconductivity (SRF'17) (Lanzhou, China, 17–21 July 2017)* pp 792–6
- [14] Matsushita T 2007 *Flux Pinning in Superconductors* vol 164 (Berlin: Springer)
- [15] Ciovati G and Gurevich A 2008 Evidence of high-field radio-frequency hot spots due to trapped vortices in niobium cavities *Phys. Rev. Spec. Top.—Accel. Beams* **11** 122001
- [16] Gurevich A 2012 Superconducting radio-frequency fundamentals for particle accelerators *Rev. Accel. Sci. Technol.* **5** 119–46
- [17] Dasgupta A, Koch C C, Kroeger D M and Chou Y T 1978 Flux pinning by grain boundaries in niobium bicrystals *Phil. Mag. B* **38** 367–80
- [18] Zerweck G 1981 On pinning of superconducting flux lines by grain boundaries *J. Low Temp. Phys.* **42** 1–9
- [19] Sung Z-H, Wang M, Polyanskii A A, Santosh C, Balachandran S, Compton C, Larbalestier D C, Bieler T R and Lee P J 2017 Development of low angle grain boundaries in lightly deformed superconducting niobium and their influence on hydride distribution and flux perturbation *J. Appl. Phys.* **121** 193903
- [20] Dhakal P, Ciovati G and Gurevich A 2020 Flux expulsion in niobium superconducting radio-frequency cavities of different purity and essential contributions to the flux sensitivity *Phys. Rev. Accel. Beams* **23** 23102
- [21] Romanenko A and Padamsee H 2010 The role of near-surface dislocations in the high magnetic field performance of superconducting niobium cavities *Supercond. Sci. Technol.* **23** 45008
- [22] Dimos D, Chaudhari P and Mannhart J 1990 Superconducting transport properties of grain boundaries in YBa<sub>2</sub> Cu<sub>3</sub>O<sub>7</sub> bicrystals *Phys. Rev. B* **41** 4038
- [23] Sung Z-H *et al* 2015 Large grain CBMM Nb ingot slices: an ideal test bed for exploring the microstructure-electromagnetic property relationships relevant to SRF *AIP Conf. Proc.* **1687** 20004
- [24] Polyanskii A A *et al* 2011 Magneto-optical study high-purity niobium for superconducting RF application *Symposium on the Superconducting Science and Technology of Ingot Niobium AIP Conf. Proc.-American Institute of Physics* vol 1352 pp 186–202
- [25] Lee P J, Polyanskii A A, Gurevich A, Squitieri A A, Larbalestier D C, Bauer P C, Boffo C and Edwards H T 2006 Grain boundary flux penetration and resistivity in large grain niobium sheet *Physica C* **441** 126–9
- [26] Wang M *et al* 2018 Investigation of the effect of strategically selected grain boundaries on superconducting properties of SRF cavity niobium *18th Int. Conf. on RF Superconductivity (SRF'17) (Lanzhou, China, 17–21 July 2017)* pp 787–91

- [27] Singer W 2016 Fabrication of elliptical SRF cavities *Supercond. Sci. Technol.* **30** 33001
- [28] Romanenko A, Barkov F, Cooley L D and Grassellino A 2013 Proximity breakdown of hydrides in superconducting niobium cavities *Supercond. Sci. Technol.* **26** 035003
- [29] Makenas B J and Birnbaum H K 1980 Phase changes in the niobium-hydrogen system I: accommodation effects during hydride precipitation *Acta Metall.* **28** 979–88
- [30] Birnbaum H K, Grossbeck M L and Amano M 1976 Hydride precipitation in Nb and some properties of NbH *J. Less Common Met.* **49** 357–70
- [31] Rauch G C, Rose R M and Wulff J 1965 Observations on microstructure and superconductivity in the Nb-H system *J. Less Common Met.* **8** 99–113
- [32] Schober T 1975 The niobium-hydrogen system—an electron microscope study. I. Room temperature results *Phys. Status Solidi* **29** 395–406
- [33] Schober T 1975 The niobium-hydrogen system—an electron microscope study. II. Low-temperature structures *Phys. Status Solidi* **30** 107–16
- [34] Schober T, Linke U and Wenzl H 1974 Metallography of the niobium hydrogen system *Scr. Metall.* **8** 805–12
- [35] Schober T and Linke U 1976 A metallographic study of the niobium-hydrogen system Part I.  $\beta$ -phase room temperature morphologies *J. Less Common Met.* **44** 63–76
- [36] Barkov F, Romanenko A, Trenikhina Y and Grassellino A 2013 Precipitation of hydrides in high purity niobium after different treatments *J. Appl. Phys.* **114** 164904
- [37] Köszegi J, Kugeler O, Abou-Ras D, Knobloch J and Schäfer R 2017 A magneto-optical study on magnetic flux expulsion and pinning in high-purity niobium *J. Appl. Phys.* **122** 173901
- [38] Grassellino A, Romanenko A, Sergatskov D, Melnychuk O, Trenikhina Y, Crawford A, Rowe A, Wong M, Khabiboulline T and Barkov F 2013 Nitrogen and argon doping of niobium for superconducting radio frequency cavities: a pathway to highly efficient accelerating structures *Supercond. Sci. Technol.* **26** 102001
- [39] Grassellino A et al 2017 Unprecedented quality factors at accelerating gradients up to  $45 \text{ MVm}^{-1}$  in niobium superconducting resonators via low temperature nitrogen infusion *Supercond. Sci. Technol.* **30** 94004
- [40] Garg P, Balachandran S, Adlakha I, Lee P J, Bieler T R and Solanki K N 2018 Revealing the role of nitrogen on hydride nucleation and stability in pure niobium using first-principles calculations *Supercond. Sci. Technol.* **31** 115007
- [41] Posen S, Checchin M, Crawford A C, Grassellino A, Martinello M, Melnychuk O S, Romanenko A, Sergatskov D A and Trenikhina Y 2016 Efficient expulsion of magnetic flux in superconducting radiofrequency cavities for high Q0 applications *J. Appl. Phys.* **119** 213903
- [42] Posen S et al 2019 Role of magnetic flux expulsion to reach  $Q_0 > 3 \times 10^4$  in superconducting rf cryomodules *Phys. Rev. Accel. Beams* **22** 32001
- [43] Polyanskii A A, Gurevich A, Pashitski A E, Heinig N F, Redwing R D, Nordman J E and Larbalestier D C 1996 Magneto-optical study of flux penetration and critical current densities in [001] tilt  $\text{YBa}_2\text{Cu}_3\text{O}_{7-\delta}$  thin-film bicrystals *Phys. Rev. B* **53** 8687
- [44] Pashitski A E, Gurevich A, Polyanskii A A, Larbalestier D C, Goyal A, Specht E D, Kroeger D M, DeLuca J A and Tkaczyk J E 1997 Reconstruction of current flow and imaging of current-limiting defects in polycrystalline superconducting films *Science* **275** 367–9
- [45] Polyanskii A A, Feldmann D M and Larbalestier D C 2003 Magneto-optical characterization techniques *Handb. Supercond. Mater.* vol 1551 ed D Cardwell and D Ginley (UK: Inst. Phys.) (<https://doi.org/10.1201/9781420034202>)
- [46] Polyanskii A, Bauer P, Lee P J, Boffo C and Edwards H 2006 A magneto-optical investigation of niobium for superconducting RF cavities *Beam Dyn. Newsl.* **39** 44–53
- [47] Li P, Abraimov D, Polyanskii A, Kametani F and Larbalestier D 2015 Study of grain boundary transparency in  $(\text{Yb}_{1-x}\text{Ca}_x)\text{Ba}_2\text{Cu}_3\text{O}$  bicrystal thin films over a wide temperature, field, and field orientation range *Phys. Rev. B* **91** 104504
- [48] Brigham Young University 2016 OpenXY (available at: <https://github.com/BYU-MicrostructureOfMaterials/OpenXY>)
- [49] Dhakal P, Chetri S, Balachandran S, Lee P J and Ciovati G 2018 Effect of low temperature baking in nitrogen on the performance of a niobium superconducting radio frequency cavity *Phys. Rev. Accel. Beams* **21** 32001
- [50] Crimp M A 2006 Scanning electron microscopy imaging of dislocations in bulk materials, using electron channeling contrast *Microsc. Res. Tech.* **69** 374–81
- [51] Zaefferer S and Elhami N-N 2014 Theory and application of electron channelling contrast imaging under controlled diffraction conditions *Acta Mater.* **75** 20–50
- [52] Zaefferer S 2000 New developments of computer-aided crystallographic analysis in transmission electron microscopy *J. Appl. Crystallogr.* **33** 10–25
- [53] Zaefferer S 2003 Computer-aided crystallographic analysis in the TEM *Adv. Imaging Electron Phys.* **125** 355–415, II-XII
- [54] Sung Z H, Lee P J, Gurevich A and Larbalestier D C 2018 Evidence for preferential flux flow at the grain boundaries of superconducting RF-quality niobium *Supercond. Sci. Technol.* **31** 45001
- [55] Balachandran S, Polyanskii A, Chetri S, Dhakal P, Su Y-F, Sung Z-H and Lee P J 2021 Direct evidence of microstructure dependence of magnetic flux trapping in niobium *Sci. Rep.* **11** 1–12
- [56] Dangwal Pandey A et al 2021 Grain boundary segregation and carbide precipitation in heat treated niobium superconducting radio frequency cavities *Appl. Phys. Lett.* **119** 194102
- [57] Rodrigues J A and Kirchheim R 1983 More evidence for the formation of a dense cottrell cloud of hydrogen (hydride) at dislocations in niobium and palladium *Scr. Metall.* **17** 159–64
- [58] Posen S et al 2018 The effect of mechanical cold work on the magnetic flux expulsion of niobium (arXiv:1804.07207)
- [59] Mansour H, Crimp M A, Gey N, Iltis X and Maloufi N 2019 Dislocation analysis of a complex sub-grain boundary in  $\text{UO}_2$  ceramic using accurate electron channelling contrast imaging in a scanning electron microscope *Ceram. Int.* **45** 18666–71
- [60] Van Gorp G J and Van Ooijen D J 1966 The influence of dislocations on superconductivity *J. Phys. Colloq.* **27** C3-51–67
- [61] Oripov B et al 2019 High-frequency nonlinear response of superconducting cavity-grade Nb surfaces *Phys. Rev. Applied* **11** 064030